Engineering and Applied Science Theses & Dissertations

McKelvey School of Engineering

Summer 8-15-2015

Photoacoustic Microscopy and Photoacoustic Computed Tomography Using High-frequency Linear Array Ultrasonic Transducers

Guo Li
Washington University in St. Louis

Follow this and additional works at: https://openscholarship.wustl.edu/eng_etds

Part of the Engineering Commons

WASHINGTON UNIVERSITY IN ST. LOUIS

School of Engineering and Applied Science
Department of Mechanical Engineering and Materials Science

Dissertation Examination Committee:
Lihong V. Wang, Chair
Mark A. Anastasio
Philip Bayly
Guy Genin
Spencer Lake
David Peters

Photoacoustic Microscopy and Photoacoustic Computed Tomography
Using High-frequency Linear Array Ultrasonic Transducers
by
Guo Li

A dissertation presented to the
Graduate School of Arts & Sciences
of Washington University in
partial fulfillment of the
requirements for the degree
of Doctor of Philosophy

August 2015
St. Louis, Missouri

Table of Contents

List of Figures

List of Abbreviations

1D	One dimensional
2D	Two dimensional
3D	Three dimensional
AR-PAM	Acoustic-resolution photoacoustic microscopy
EIR	Electrical impulse response
FBP	Filtered back-projection
FOV	Field of view
FWHM	Full width at half maximum
HIFU	high-intensity focused ultrasound
ILRT-PACT	Inverse linear Radon transformation photoacoustic computed tomography
MAP	Maximum amplitude projection
MFOR-PAM	Multifocal optical-resolution photoacoustic microscopy
NA	Numerical aperture
OR-PAM	Optical-resolution photoacoustic microscopy
PA	Photoacoustic
PACT	Photoacoustic computed tomography
PAE	Photoacoustic endoscopy
PAM	Photoacoustic microscopy
PAT	Photoacoustic tomography
PRR	Pulse repetition rate
SNR	Signal-to-noise ratio
sO_2	Oxygen saturation of hemoglobin
SOS	Speed of sound

<u>Acknowledgments</u>

I gratefully acknowledge the continuous guidance, encouragement, and support of my advisor Dr. Lihong Wang, the Gene K. Beare Distinguished Professor in the Department of Biomedical Engineering, Washington University in St. Louis. Without his constructive advice and support, I would not have been able to complete this work.

This dissertation is based on teamwork with many lab members and collaborators. I am grateful to Dr. Konstantin Maslov, Dr. Jun Xia, Dr. Lidai Wang, Lei Li, Yong Zhou and Liren Zhu for their contributions, as well as Dr. Liang Song and Dr. Junjie Yao for their inspiring discussions. I also appreciate everyone who has helped me at Washington University.

<div align="right">Guo Li</div>

Washington University in St. Louis

August 2015

Dedicated to

my wife Juan Wang, my parents, and my parents in law

ABSTRACT OF THE DISSERTATION

Photoacoustic Microscopy and Photoacoustic Computed Tomography

Using High-frequency Linear Array Ultrasonic Transducers

by

Guo Li

Doctor of Philosophy in Mechanical Engineering

Washington University in St. Louis, 2015

Professor Lihong V. Wang, Chair

Photoacoustic tomography (PAT) is a highly promising imaging technology which forms images by detecting the induced pressure waves resulting from pulsed light absorption in biological tissues. Because the excitation source is light, PAT is a very safe, non-ionizing, and non-carcinogenic imaging technology. In biomedicine, PAT has the unique advantage of probing endogenous optical absorbers at different length scales with 100% relative sensitivity. With such scalability, PAT can image anatomical, functional, metabolic, molecular, and genetic contrasts of vasculature, hemodynamics, oxygen metabolism, biomarkers, and gene expression. Among several implementations of PAT, optical-resolution photoacoustic microscopy (OR-PAM) and photoacoustic computed tomography (PACT) are two of the most widely used. OR-PAM can achieve optical diffraction limited spatial resolution with maximum imaging depths up to one transport mean free path (~1 mm in biological tissue). PACT can achieve several centimeters imaging depth in tissue by employing ultrasonic array detectors and inverse algorithms. This dissertation aims to improve the functionality of OR-PAM using a high-frequency linear

ultrasonic array, and to advance the performance of linear-array PACT to full view angle capability and higher resolution.

The first part of this dissertation describes the technological advancement of multifocal optical-resolution photoacoustic microscopy (MFOR-PAM). Compared with single-focus OR-PAM, 1D multifocal OR-PAM utilizes both multifocal optical illumination and an ultrasonic transducer array, significantly increasing the imaging speed. We present a reflection-mode 1D multifocal OR-PAM system based on a 1D microlens array that provides multiple foci as well as an ultrasonic transducer array that receives the excited photoacoustic waves from all foci simultaneously. Using a customized microprism to reflect the incident laser beam to the microlens array, the multiple optical foci are aligned confocally with the focal zone of the ultrasonic transducer array. Experiments show the reflection-mode 1D multifocal OR-PAM is capable of imaging microvessels *in vivo*, and it can image a $6 \times 5 \times 2.5$ mm^3 volume at 16 μm lateral resolution in ~2.5 min, limited by the signal multiplexing ratio and laser pulse repetition rate. While 1D-MFOR-PAM accelerates the scan in only one direction, a two-dimensional MFOR-PAM (2D-MFOR-PAM) fully explores the advantage of a 2D microlens array. By scanning a small range of 250 μm × 250 μm, we eventually obtained a large field of view of 10 mm × 10 mm in ~50 seconds, with a spatial resolution of 15.2 μm.

The second part of this dissertation describes methods of increasing the view angle of linear-array PACT, which suffers from a limited view. While rotating either the transducer array or the imaging objects circularly enables full-view linear-array PACT, this process is time consuming. Here we propose two innovative methods to increase the view angle. The first method is to triple the detection view angle by using two planar acoustic reflectors placed at 120 degrees to each other. Without sacrificing the imaging speed, we form two virtual linear transducer arrays,

adding two vantage points. Experimental results show the detection view angle of the linear-array PACT was increased from 80 to 240 degrees. The second method is an ultrasonic thermal encoding approach that is universally applicable to achieve full-view imaging with linear-array PACT. We demonstrate full-view *in vivo* vascular imaging and compare it to the original linear-array PACT images, showing dramatically enhanced imaging of arbitrarily oriented blood vessels.

The last part of the dissertation describes the development of algorithms for linear-array PACT. The first proposed algorithm is a multi-view Hilbert transformation, which provides accurate optical absorption for full-view linear-array PACT. A multi-view high-frequency PACT imaging system was implemented with a commercial 40-MHz central frequency linear transducer array. By rotating the object through multiple angles with respect to the linear transducer array, we acquired full-view photoacoustic pressure measurements. The in-plane spatial resolution of this full-view linear-array PACT was quantified to be isotropically 60 µm within a 10×10 mm^2 field of view. The system was demonstrated by imaging both a leaf skeleton and a zebrafish *in vivo*. The second algorithm is an inverse linear Radon transformation (ILRT), which allows linear-PACT to achieve isotropic resolution at all depth planes. Images of microspheres acquired by inverse linear Radon transformation PACT (ILRT-PACT) demonstrate that our technique improves the elevational resolution by up to 9.4 times over that of a single linear scan. The technique is further demonstrated through *in vivo* imaging of the mouse brain through an intact scalp.

Chapter 1: Introduction

1.1 Photoacoustic Tomography

In 1880, Alexander Graham Bell discovered the photoacoustic effect, in which light absorption in matter causes pressure rises propagating as acoustic waves [1]. Spurred by the development of lasers and computers, photoacoustic tomography (PAT) has developed rapidly in the past decade. PAT forms images by detecting the induced pressure waves resulting from pulsed light absorption in biological tissues. Because PAT uses light, it is a very safe, non-ionizing, and non-carcinogenic imaging technology. Although both conventional ultrasound imaging and PAT are based on ultrasonic detection, the former is sensitive to mechanical contrasts and the latter to optical and thermoelastic contrasts. These contrasts can be, but are not limited to, the following: oxy-hemoglobin, deoxy-hemoglobin, melanin, lipid, water, DNA, and RNA. Currently, PAT can image anatomical, functional, metabolic, molecular, and genetic contrasts of vasculature, hemodynamics, oxygen metabolism, biomarkers, and gene expression [2].

Different PAT implementations can achieve scaled spatial resolutions at useful imaging depths in tissue, while maintaining a high depth-to-resolution ratio (typically ~200). PAT has three major implementations: focused-scanning photoacoustic microscopy (PAM) [3-6], photoacoustic computed tomography (PACT) [7, 8], and photoacoustic endoscopy (PAE) [9]. PAM and PAE usually aim to image millimeters deep with micrometer scale resolution, and PACT can image tissues at both microscopic and macroscopic scales. Details of the three major implementations and their sub-implementations are discussed in Wang and Hu [2].

In PAM, the dual foci of the optical illumination and ultrasonic detection are usually confocally configured to maximize sensitivity. For PAM with a single-element ultrasonic transducer, each laser pulse excitation generates a one-dimensional (1D) image which contains the depth information, and a two-dimensional (2D) transverse scan generates a three-dimensional (3D) image. The axial resolution is provided by the time-resolved ultrasonic detection, and it can be estimated as 0.88 v_s/B if the impulse response of the ultrasonic transducer has a Gaussian envelope. Here v_s is the speed of sound and B is the ultrasonic transducer bandwidth, which is approximately proportional to the central frequency. The lateral resolution is determined by the overlap of the dual foci. Quantitatively, the axial and lateral resolutions are defined as the corresponding full width at half maximum (FWHM) of the system response to a point target. Depending on whether the optical or ultrasonic focus is finer, PAM can be further classified into optical-resolution PAM (OR-PAM) or acoustic-resolution PAM (AR-PAM). OR-PAM implements the PAM configuration by focusing the illumination through an objective lens. Thus OR-PAM can achieve optical-diffraction limited lateral resolution with penetration depths up to the optical transport mean free path (~1 mm in biological tissue). In contrast, AR-PAM can image tissue at depths beyond the optical diffusion limit, up to a few millimeters deep.

Different from PAM, which usually images only millimeters deep, photoacoustic computed tomography (PACT) can be used in both microscopic and macroscopic imaging by employing an inverse algorithm to reconstruct images. Xu and Wang reported a universal back-projection formula for three types of imaged geometries: planar, spherical, and cylindrical surfaces [10]. This universal back-projection formula was used in this research to reconstruct images. To accelerate the imaging speed, an array of ultrasonic transducers was used. Based on the configuration of the ultrasonic transducer array elements, array PACTs are classified as linear-

array PACT or circular-array PACT. This dissertation work focuses on linear-array PACT. Because most ultrasonic transducer arrays are 1D, the 2D resolutions in the imaging plane are derived from reconstruction, and the orthogonal (elevational) resolution comes from cylindrical acoustic focusing. Currently, only low-frequency ultrasonic transducer arrays have been used for PACT imaging. Correspondingly, the reconstructed image resolution in the imaging plane for these low-frequency PACT systems is typically larger than 100 μm. As a rule of thumb, the higher the central frequency of the transducer array, the higher the reconstructed resolution in the imaging plane.

1.2   Outline of the Dissertation

This work aims to improve the functionality of OR-PAM using a high-frequency linear ultrasonic array, and to advance the performance of linear-array PACT to full view angle capability and higher resolution. First, we redesigned a one-dimensional multifocal OR-PAM (1D-MFOR-PAM) system, making it work in reflection mode, and a two-dimensional multifocal OR-PAM (2D-MFOR-PAM) system with 1600 times faster than a single-focus OR-PAM (Chapter 2). Second, we explored broadening the view angle of linear-array PACT, which suffers from limited view (Chapter 3). Broadened view PA images show more features and yield more accurate details in tissue. Third, we explored both technical improvements and algorithms to improve the image quality and spatial resolutions (Chapter 4). Finally, the dissertation presented is summarized in Chapter 5, and directions for future work are presented.

Chapter 2: Multifocal Optical-resolution Photoacoustic Microscopy

This chapter describes the technical development of one-dimensional and two-dimensional multifocal optical-resolution photoacoustic microscopy (MFOR-PAM). The achieved 1D-MFOR-PAM works in reflection mode, eliminating the thickness limitation of samples. The 2D-MFOR-PAM achieves 1600 times higher imaging speed than the single-focus OR-PAM. Part of this chapter has been published in the Journal of Biomedical Optics [11].

2.1   Reflection-mode Multifocal Optical-resolution Photoacoustic Microscopy

Background   Photoacoustic microscopy (PAM) is a mode of photoacoustic tomography (PAT), which offers high sensitivity to optical contrast in biological tissues [12]. Optical-resolution PAM (OR-PAM) is implemented by focusing the illumination through an objective lens; thus OR-PAM can achieve optical diffraction limited lateral resolution with maximum imaging depths up to one transport mean-free path (~1 mm in tissue) [4, 13]. OR-PAM can provide structural imaging, and metabolic imaging [14, 15]. Various kinds of OR-PAM have also been explored to meet specific requirements, such as high speed [16], high resolution [17, 18], deep imaging depth [13], and handheld operation [19].

For OR-PAM, high imaging speed is always desirable because it enables us to observe dynamic biological processes while mitigating motion artifacts. For most OR-PAM systems based on both a single optical focus and a single-element ultrasonic transducer in confocal configuration, mechanical raster scanning along two lateral directions provides limited volumetric imaging speeds. Although optical scanning (i.e., scanning using galvo mirrors) can improve the speed greatly, it is usually used with an unfocused or a single-axis focused ultrasonic transducer, which

results in a limited field of view (FOV) or compromised signal-to-noise ratio (SNR). Moreover, the volumetric imaging speed for OR-PAM with either mechanical or optical scanning is eventually limited by the laser pulse repetition rate (PRR). Thus to achieve high imaging speed, lasers with high PRR (~100 kHz, or even faster) are employed [16, 19]. Currently, lasers with such high PRR usually lack the wavelength tunability, which is essential for imaging of some physiological functions, such as the oxygen saturation of hemoglobin (sO$_2$). Moreover, high PRR translates to high average optical power, which may produce excessive tissue heating. Our lab previously reported a multifocal OR-PAM (MFOR-PAM) with ~20 times faster imaging speed (without considering the multiplexing effect) than a single-focus OR-PAM [20]; thus it relieves the demand for a high laser PRR. Besides the imaging speed improvement, the sO$_2$ measurement capability makes MFOR-PAM potentially promising in clinical and preclinical applications. However, the original MFOR-PAM works in transmission mode, only suited for imaging thin biological samples. Therefore, it is necessary to develop reflection-mode MFOR-PAM.

Methods We implemented the reflection-mode MFOR-PAM by placing a microlens array directly below the ultrasonic transducer array, with both immersed in water, as shown in Fig. 2.1. To get one-dimensional (1D) multifocal optical illumination, the microlens array (250 μm pitch and 1.2 mm focal length in air, 11-1640-123-000, SUSS MicroOptics, Switzerland) was precisely cut by Biomedical-Optics LLC to 0.5 mm wide and 10 mm long. Due to the limited detection range of the ultrasonic transducer array, only 20 microlenses were used to provide 20 focused optical illumination spots along the lateral axis. At a laser wavelength of 570 nm, Zemax (Radiant Zemax LLC) simulation shows that the water-immersed microlens can produce a diffraction-limited focus with a radius of ~7 μm at the waist and an effective focal length of 3.4 mm. The centers of the microlens array and the ultrasonic transducer array were aligned in both

the elevational (x axis in Fig. 2.1) and lateral (y axis in Fig. 2.1) directions. The microlens array was carefully adjusted so that the optical foci of the microlens array and the cylindrical focus of ultrasonic transducer array overlap. To reflect the laser beam, which is incident from the elevational side, a customized microprism (0.5 mm wide × 0.5 mm high × 7 mm long, Biomedical-Optics LLC) was used. The microprism and the microlens array were aligned on their centers and glued together with optically transparent adhesive. The ultrasonic transducer array consisted of 48 elements with 100 μm pitch, and each element (82 μm × 2 mm) had a central frequency of 30 MHz and a 70% receiving-only bandwidth. A tunable dye laser (Cobra, Sirah, Germany) pumped by a Q-switched Nd:YLF laser (INNOSLAB, EdgeWave, Germany) provided photoacoustic excitation at 1.35 kHz. Technical details about the ultrasound array system can be found in our previous publications [20, 21].

In this reflection-mode MFOR-PAM, the PA wave was partially reflected by the microlens array when propagating to the transducer. Fig. 2.1(c) shows the dimensions that were used to estimate the fractional PA wave loss, which is $w'/w_2 = w_1 f_2/(w_2 f_1)$. Here we neglect the acoustic diffraction effect because the acoustic wavelength is much smaller than the width of the microlens array. With $f_1 = 3.4$ mm, $w_1 = 0.5$ mm, $f_2 = 8.2$ mm, and $w_2 = 2.0$ mm, the fraction of acoustic energy reaching the transducer array, was $1 - w'/w_2$, equal to ~40%. Also, this design allows us to extend the microscope's working distance to the whole optical focal length, which is convenient in biomedical imaging applications.
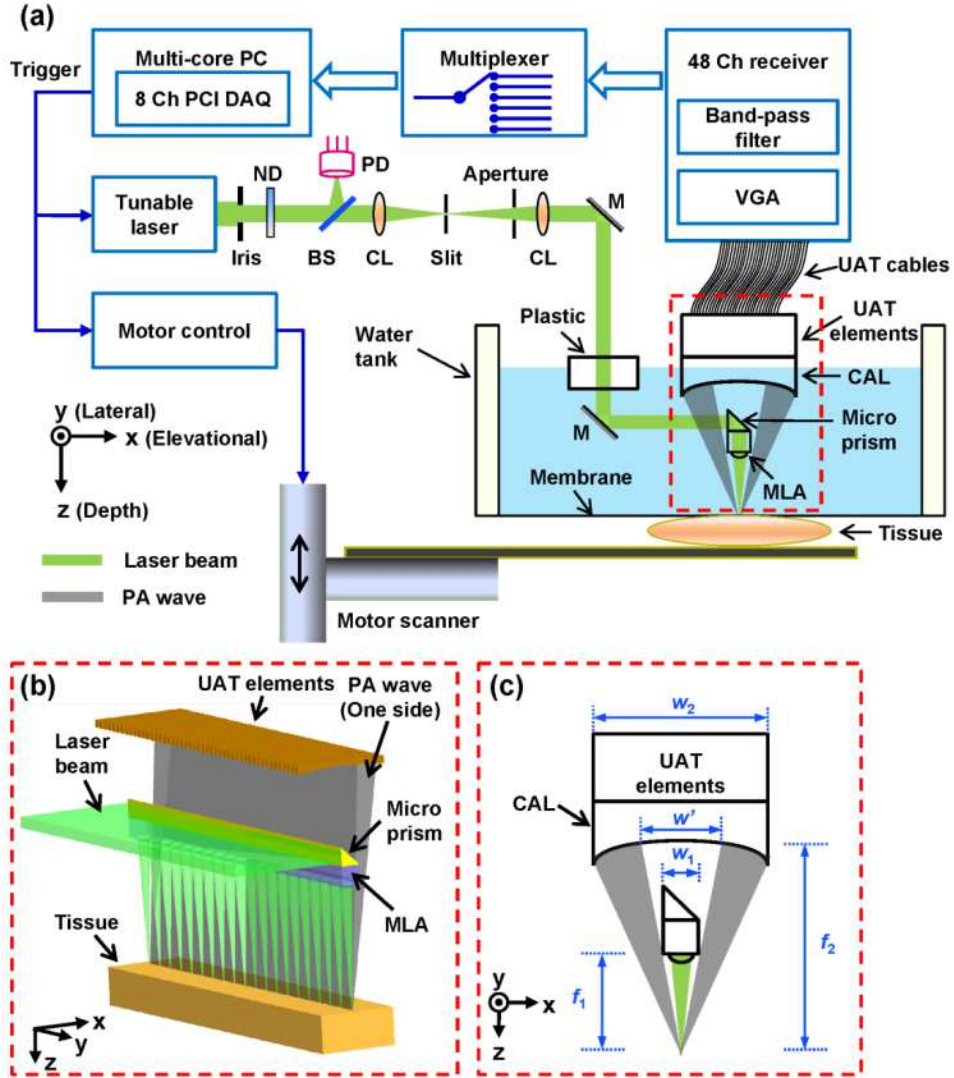
Figure 2.1 Configuration of the reflection-mode MFOR-PAM system. (a) Schematic of the whole system. ND, neutral density filter; BS, beam sampler; PD, photodiode; CL, convex cylindrical lens; M, mirror; UAT, ultrasonic transducer array; CAL, cylindrical acoustic lens; MLA, microlens array; VGA, variable gain amplifier. (b) 3D view of the components in the dashed box of (a). To show the configuration more clearly, only one side of the PA wave is presented. (c) Dimensions used to estimate the PA wave receiving percentage of the ultrasonic transducer array. f_1 and w_1, focal length and width of the microlens array immersed in water; f_2, focal length of the cylindrical acoustic lens; w_2, width of the transducer element; w', portion of the width that cannot receive PA waves.

Results In MFOR-PAM, the lateral resolution and elevational resolution are the same because of the symmetric property of the optical focus [20]. Therefore, hereafter we use "lateral resolution" to denote both the lateral resolution and elevational resolution. To quantify the lateral

7

resolution of the reflection-mode MFOR-PAM, we imaged two crossed 6-μm-diameter carbon fibers, using a scanning step size of 2 μm. Fig. 2.2(a) shows the maximum amplitude projection (MAP) along the depth direction for the carbon fibers. Fig. 2.2(b) shows the PA signal amplitude along the dashed line *x'* in (a). The full width at half maximum (FWHM) of the curve in Fig. 2.2(b) measures 16 μm, which represents the lateral resolution of the system. Due to the water immersion, this value is lower than the 10 μm lateral resolution of the transmission mode MFOR-PAM. Although there is ~60% loss of the PA wave compared with the transmission mode MFOR-PAM, the signal-to-noise ratio (SNR) in Fig. 2.2(a) still reaches 19 dB, which is adequate for imaging micro blood vessels. The axial resolution, which is determined by the receiving ultrasonic bandwidth of the transducer, is ~25 μm, as reported in previous publications [20, 21]. The penetration depth of the reflection-mode MFOR-PAM was also studied by imaging a 250 μm-diameter black needle obliquely inserted into the leg of a nude mouse (Hsd, Athymic Nude-Foxnlnu, Harlan Co.). With time gain compensation, Fig. 2(c) shows that the black needle can still be observed 0.7 mm beneath the skin surface of the mouse leg. Compared to the maximum imaging depths of other OR-PAM systems (up to 1.2 mm) [4, 16], this depth is shallower because the microlens array reflects ~60% of the PA wave. However, this maximum imaging depth is still sufficient for observations of many shallow structures.
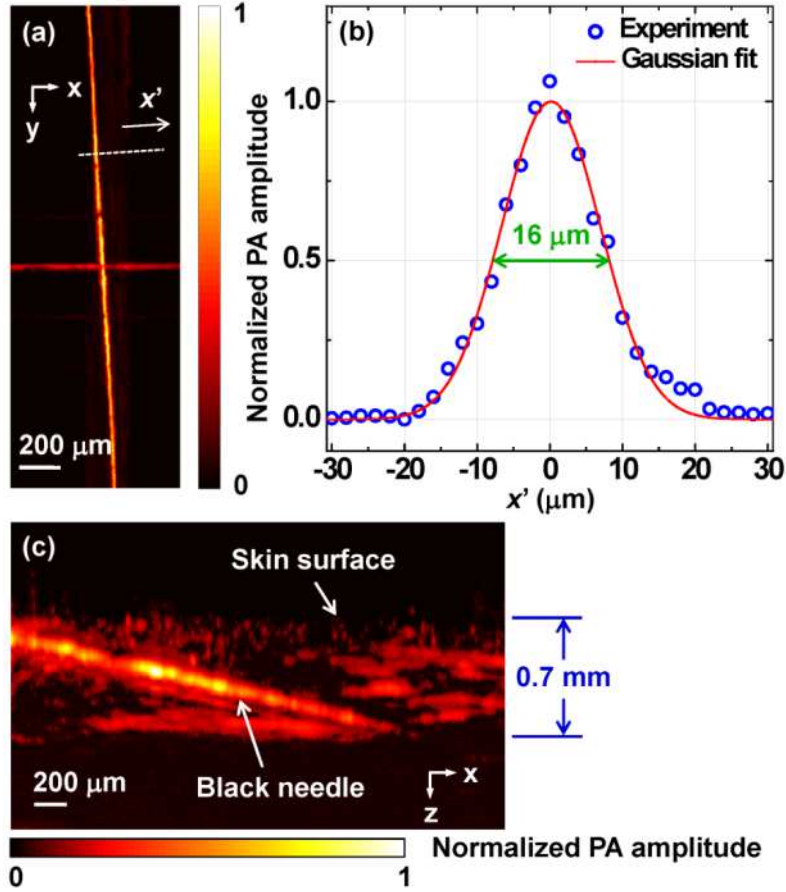
Figure 2.2 Characteristics of the reflection-mode MFOR-PAM. (a) MAP image of two crossed 6-μm-diameter carbon fibers. (b) PA amplitude distribution along the dashed line in (a). Blue circles are the experimental data, and the red curve is the Gaussian fit. (c) *In vivo* photoacoustic image of a black needle inserted obliquely into the leg of a nude mouse.

Fig. 2.3(a) shows an *in vivo* MAP image of a mouse ear microvasculature acquired by the reflection-mode MFOR-PAM system. The MAP image was processed by the 2×2 Gaussian low pass filter. The laser wavelength was set to the isosbestic wavelength of 570 nm, where hemoglobin has high absorption. Fig. 2.3(b) shows a snapshot from the 3D animation. Microvessels were clearly imaged in both the MAP image and the 3D animation. The imaging time to acquire the data set of Fig. 2.3 (600×500×200 voxels) was ~2.5 min. The incident laser

9

energy on each microlens was limited to ~62 nJ/pulse, and the laser fluence on the ear surface was estimated to be 16 mJ/cm², lower than the ANSI limit 20 mJ/cm².
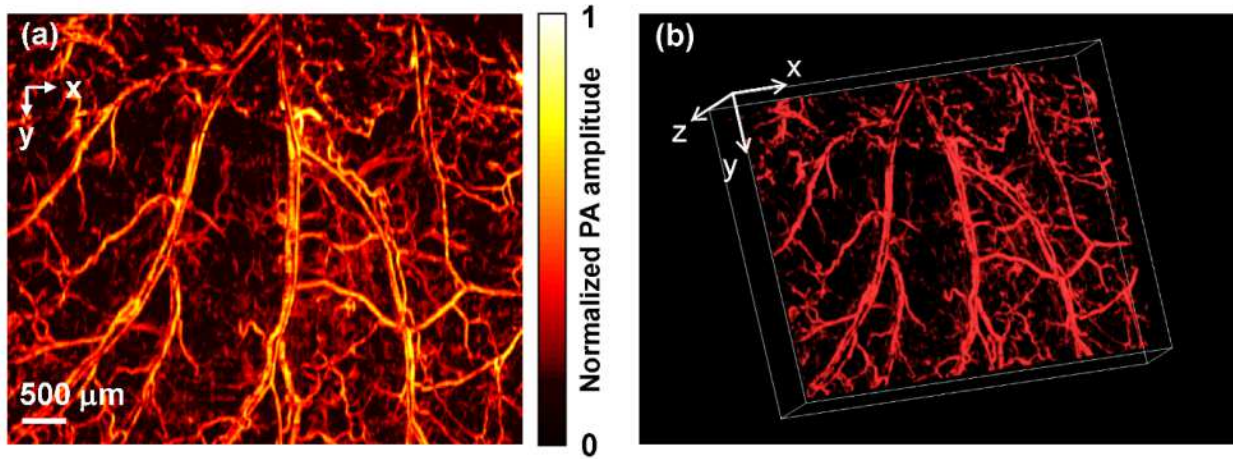
Figure 2.3 *In vivo* photoacoustic images of a nude mouse ear. (a) MAP image. (b) Snapshot from the 3D animation, showing the microvasculature in (a).
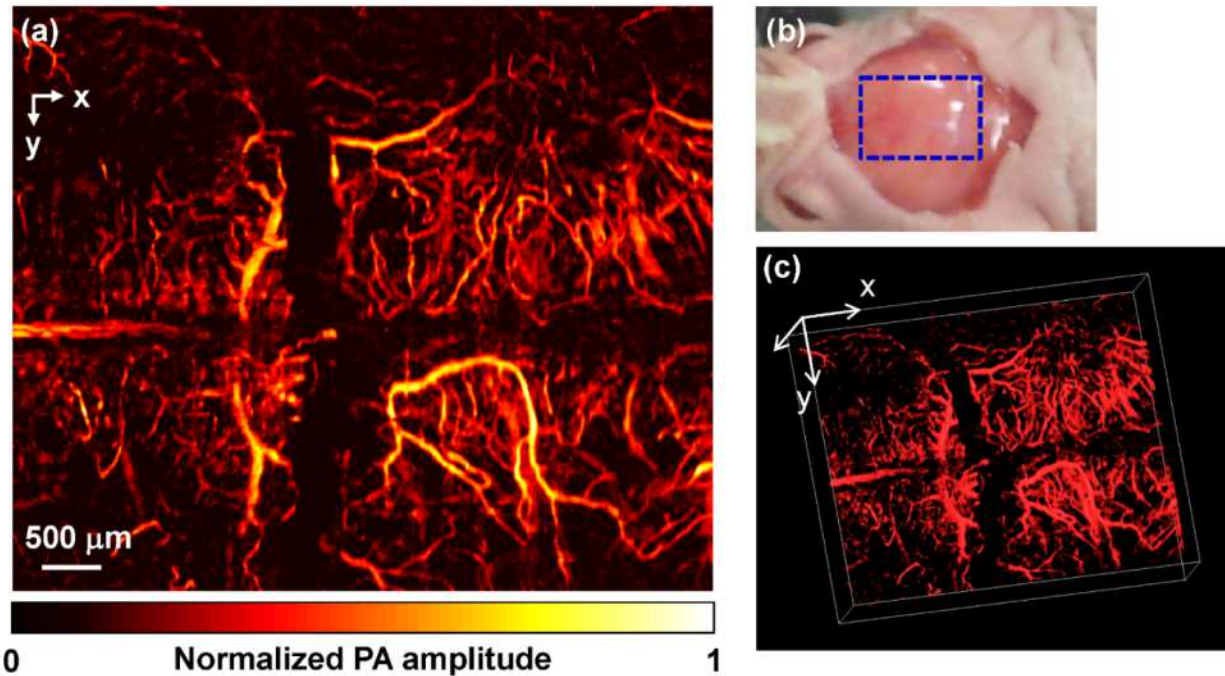
Figure 2.4 *In vivo* trans-cranial photoacoustic images of a nude mouse brain with the skin removed. (a) MAP image of the brain. (b) Photograph of the mouse brain with skin removed. The dashed box is the imaging area presented in (a). (c) Snapshot from the 3D animation showing the structure in (a).

With the flexibility of reflection mode, the *in vivo* PA image of a nude mouse brain was also acquired. Fig. 2.4(a) shows the MAP image of a living adult mouse brain. The MAP image was processed by the 2×2 Gaussian low pass filter. The skin of the mouse brain was removed, but the skull was kept intact, as shown in Fig. 2.4(b). From Fig. 2.4(a), the microvessels can be clearly observed, even though the intact skull attenuated both the incident light and the PA wave. Fig. 2.4(c) is a snapshot from the 3D animation, showing the mouse brain from various viewing angles. The 3D animation shows the curved shape of the mouse brain.

Discussion   Potentially the imaging speed can be further improved by eliminating the 6:1 multiplexer, and using a higher PRR laser. Optical scanning within one pitch in the lateral direction can further improve the imaging speed by several times. A more densely packed microlens array with a smaller pitch might improve the imaging speed, but this usually means a shorter working distance if we want to maintain the (numerical aperture) NA or lateral resolution. Other multifocal designs might be developed to provide both a high NA and long working distance.

2.2   Two-dimensional Multifocal Optical-resolution Photoacoustic Microscopy Based on a Liner Ultrasound Transducer Array

Background Most reported OR-PAMs use a confocal setup with a single optical focus and single acoustic focus [3, 4, 13, 16, 18, 22-27]. Single-focus OR-PAM can acquire an A-line signal at each laser pulse shot, and by performing a two-dimensional (2D) raster scan, a three-dimensional (3D) image can be acquired. While the cost of the single-focus OR-PAM is low, the imaging speed is limited by the dense raster scan. To accelerate the imaging speed, a high repetition rate laser and a high-speed optical scanning method have been used. For instance,

using a 100 kHz repetition rate laser, Yao et al. [16] reported an OR-PAM that utilized a lab-made water-immersible microelectromechanical systems (MEMS) scanning mirror (MEMS-OR-PAM). The MEMS-OR-PAM achieved a C-scan rate of 0.8 Hz with a field of view (FOV) of 2 mm × 5 mm. However, the C-scan rate will decrease correspondingly when the FOV is increased. To maintain the scanning speed for a larger FOV, a higher repetition rate laser or a faster scanning method must be used, both are technically challenging.

Alternatively, we can accelerate the scan speed by using multiple optical foci to simultaneously excite multiple locations and then detecting excited photoacoustic waves with an ultrasonic transducer array. The advantage of the multifocal method is that the scan speed can be improved without increasing the laser repetition rate. A microlens array is a convenient way to obtain multiple optical foci. Song et al. [20] reported the first multi-focal optical-resolution photoacoustic microscopy (MFOR-PAM) with a one-dimensional (1D) microlens array consisting of 20 microlenses in a line. Experiments done in the transmission mode showed that the MFOR-PAM was 20 times faster than a single-focus OR-PAM with mechanical raster scan. A reflection-mode MFOR-PAM with the same 1D microlens array has also been reported [11]. However, the 1D microlens array accelerates the scan in only one direction, and the other direction's scanning speed remains unchanged. MFOR-PAM employing a 2D microlens array and a ring transducer array was recently reported to address this limitation [27]. The 2D-MFOR-PAM fully explores the advantage of a 2D microlens array. However, the ring transducer array is usually customized and costly. Moreover, the ring transducer array requires accessibility from all sides of the target, which limits the size of the target that can be imaged. In contrast, a linear transducer array is commercially available at low cost, and it can detect PA waves from a single

side of the target. In this section, we reported the development of a linear transducer array-based 2D-MFOR-PAM.

Methods   The setup of the 2D-MFOR-PAM is shown in Fig. 1(a). A 20 Hz laser beam (Brilliant, Quantel, USA) with 532 nm wavelength was directed onto a 2D microlens array (18-00030, SUSS MicroOptics). The microlens array had a 40 × 40 grid of spherical microlens with 250 μm center-to-center spacing. Each microlens had a diameter of a few microns less than 250 μm, and a radius of curvature of 297 μm. Zemax (Radiant Zemax LLC) simulation gave an NA of 0.22 and a focus size of 2.4 μm in air. However, the focal length of each microlens was only 0.54 mm, too short for biomedical imaging. Therefore we used a camera macro lens (50mm F2.8 EX DG, Sigma) to extend the working distance of the microlens array. The magnification of the macro lens was adjusted to 1:1, and we carefully aligned the microlens array and the macro lens to relay multiple optical foci to the other side of the macro lens. In this way we obtained a much longer working distance of around 4 cm. Because the NA of the camera lens (0.13, corresponding to the magnification of 1:1) was smaller than the NA of the microlens, the relayed focal spot size was mainly determined by the NA of the camera lens, and was approximately 5 μm. A commercial cylindrically focused linear ultrasonic transducer array with 256 elements (MS400, 30 MHz central frequency, 20 MHz bandwidth, Visualsonics Inc., Canada) was the photoacoustic detector. The focal length of the cylindrical acoustic lens was 9 mm. The average laser intensity was ~18 mJ/cm^2 on the target's surface, which is less than the ANSI (American National Standards Institute) safety limit (20 mJ/cm^2). A commercial photoacoustic imaging platform (Vevo LAZR, Visualsonics Inc., Canada) was used to acquire photoacoustic images. Due to the four-to-one multiplexing in the data acquisition system, the B-scan frame rate was 5 frames/sec, with a laser repetition rate of 20 Hz. Two mechanical translation stages scanned the

whole optical assembly (including the aperture, microlens array, and camera lens) along the x and y directions.
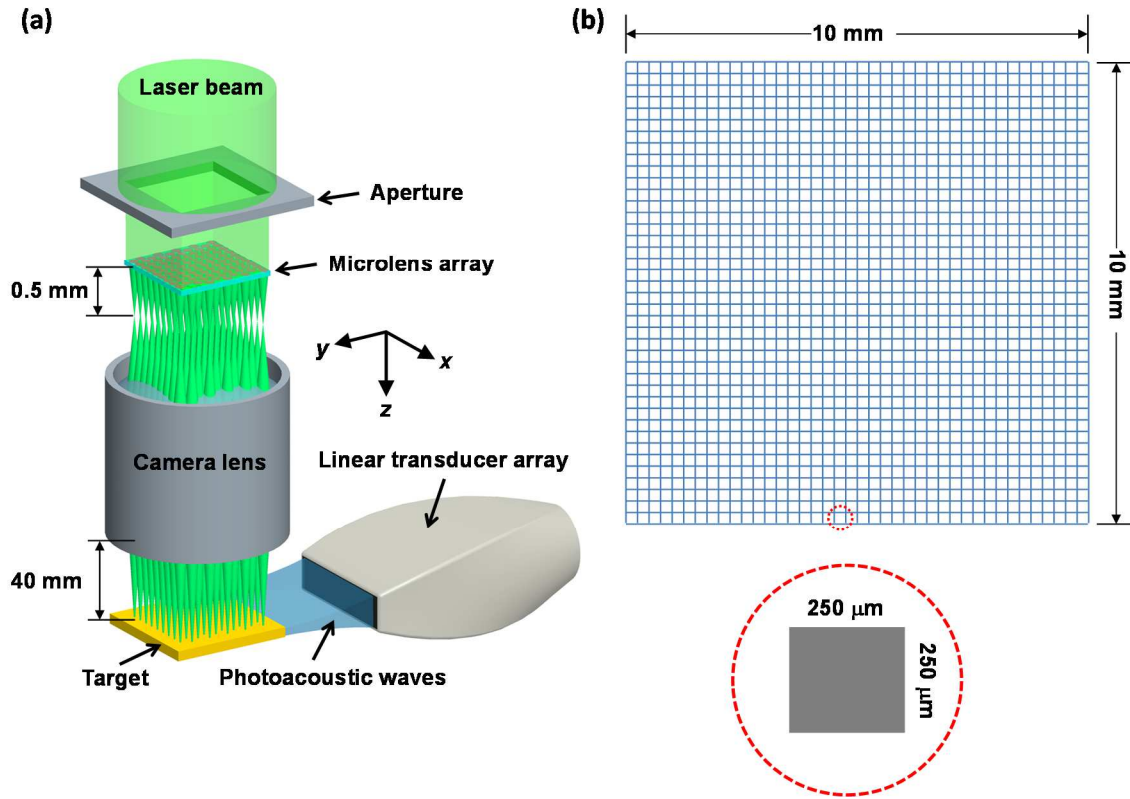
Figure 2.5 Schematic drawing of the 2D-MFOR-PAM system with a linear transducer array (not to scale). (a) 3D view of the system. (b) Field of view (10 mm × 10 mm), and the scan range (250 μm × 250 μm) of the system.

To reconstruct the optical-resolution image, we processed the raw data through three steps. In the first step, we reconstructed 2D images corresponding to all scanning positions, using the filtered backprojection (FBP) algorithm. In the second step, we constructed 2D masks for each scanning position. In each 2D mask, only pixels corresponding to optical foci locations have a value of one, and other pixel values are set to zero. By multiplying the 2D image acquired in the first step with its corresponding 2D mask pixel-wise, we formed an image revealing the optical absorption in the optical foci locations. In the last step, we combine all the images in the second step to get a final optical-resolution PAM image.

Results We quantified the spatial resolution of the 2D-MFOR-PAM by imaging a 6-μm-diameter carbon fiber glued on top of an agar gel. The microlens scanned across the carbon fiber in the *y* direction at 2.5 μm per step. We then reconstructed a PA image at each scanning step and identified a pixel corresponding to the center of the carbon fiber. We plotted the PA intensity of that pixel over different scanning positions to get the intensity profile. Fig. 2 shows the 1D profile of the PA amplitude along the *y* direction. By taking a Gaussian fit on the profile, we found a full width at half maximum (FWHM) value of 15.2 μm, which is the spatial resolution of the 2D-MFOR-PAM system. The spatial resolution is worse than the estimated focus spot size (~5 μm), possibly due to the low beam quality and mechanical instability. Having quantified the spatial resolution, we accordingly chose a scanning step size of 15.6 μm. For a total scan range of 250 μm × 250 μm, there were 256 scan steps for each image. Due to four-to-one multiplexing, the scanning motors moved one step after every four laser pulses. With five frames/sec B-scan frame rate, the whole scan took 51 sec, with a FOV of 10 mm × 10 mm (size of the microlens array).
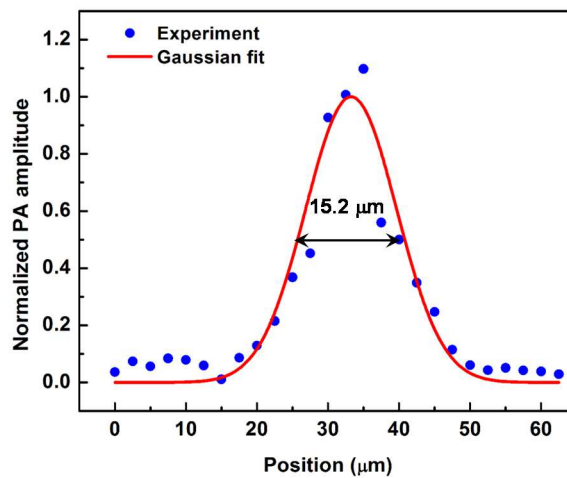
Figure 2.6 Line-spread function used to measure the in-plane spatial resolution of the 2D-MFOR-PAM system.

15

We imaged the ear of a nude mouse (Hsd, Athymic Nude-Foxnlnu, Harlan Co.) *in vivo*. All animal work was performed in compliance with Washington University's institutional animal protocols. After the experiment, we reconstructed the final image using the aforementioned three-step method. Fig. 3(a) shows a 2D image of the mouse ear in the first scanning step. A 2D mask with green dots indicates the locations of optical foci. Fig. 2(b) shows the final high-resolution image obtained by combining masked 2D images at all scanning steps. The capillaries of the mouse ear are clear.
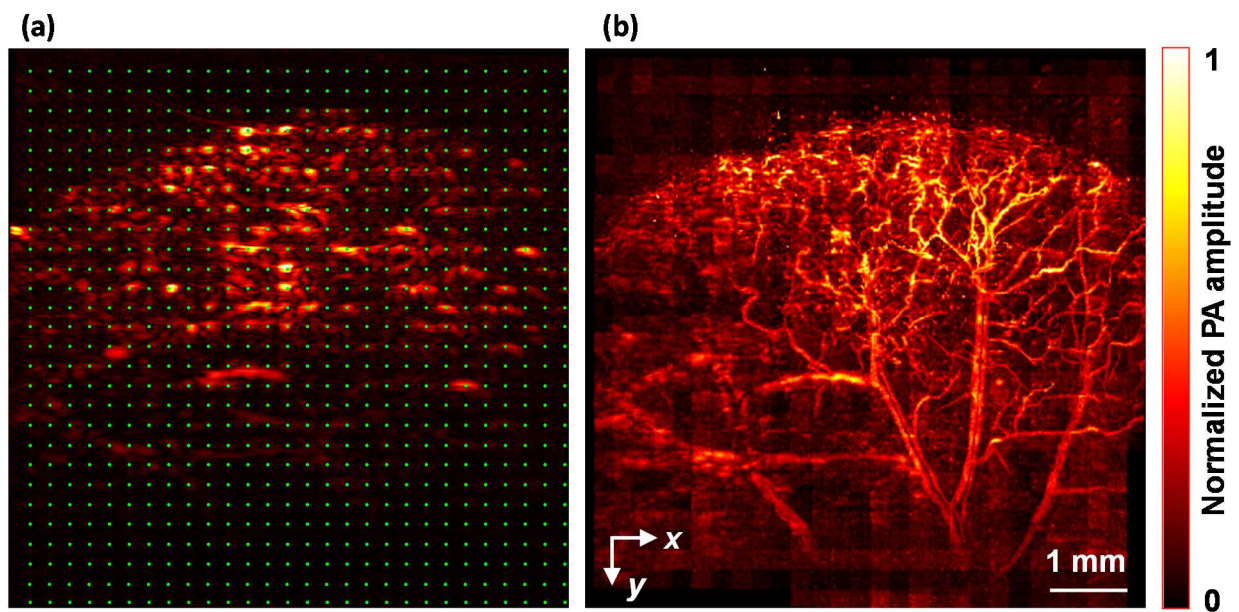
Figure 2.7 Images of a mouse ear *in vivo*. (a) Reconstructed PA image corresponding to the first scanning step. Green dots indicate the optical foci. (b) Final reconstructed optical-resolution image obtained by combining all masked PA images.

Conclusions Even with the current laser repetition rate of 20 Hz, the imaging speed of the 2D-MFOR-PAM is already comparable to the single-focus MEMS-OR-PAM with a laser repetition rate of 100 kHz. MEMS-OR-PAM takes at least 12.5 sec to image a 10 mm × 10 mm FOV,

according to the reported imaging speed (1.25 sec for 2 mm × 5 mm FOV). This time is almost the same as the time of 2D-MFOR-PAM without the four-to-one multiplexing, which is 12.75 sec. With a higher laser repetition rate and optical scanning, the imaging speed of the 2D-MFOR-PAM can be further improved to video rate, which is desirable for monitoring real-time hemodynamic and neural activity.

2.3　Conclusions

We have developed a reflection-mode 1D-MFOR-PAM system using a microlens array and a linear ultrasonic transducer array. The reflection-mode MFOR-PAM was capable of acquiring volumetric PA images *in vivo*, with a lateral FWHM resolution of 16 μm, axial resolution of ~25 μm, and *in vivo* penetration depth up to 0.7 mm. Due to the combination of multiple optical foci and the ultrasonic transducer array, the lateral scanning range was reduced to only one pitch of the microlens array; thus the imaging speed was much faster than the single-focus OR-PAM with mechanical scanning.

Because 1D-MFOR-PAM accelerates the scan along only one direction, we also developed a linear transducer array-based 2D-MFOR-PAM system that fully explores the potentials of a 2D microlens array and provides wide-field optical-resolution images at a high imaging speed. The scanning range was only 250 μm × 250 μm, and the FOV was 10 mm × 10 mm. *In vivo* mouse ear images were successfully acquired using the 2D-MFOR-PAM system, with a spatial resolution of 15.2 μm.

Chapter 3: Broadening the View Angle of Linear-array Photoacoustic Computed Tomography

This chapter describes the technical innovations for broadening the view angle of linear-array PACT, which suffers from a limited view. Broadening the view angle will allow linear-array PACT to present features more accurately. Parts of this chapter have been published in Quantitative Imaging in Medicine and Surgery [28], and Optica [29] (Coauthor with equal contribution).

3.1 Tripling the Detection View Angle Using Two Planar Acoustic Reflectors

Background Photoacoustic tomography (PAT) forms images by detecting photoacoustic waves originating from thermal expansion caused by pulsed light absorption in biological tissues. Because acoustic scattering is several orders of magnitude less than optical scattering in biological tissue, PAT can acquire images of optical absorption at a depth beyond the optical diffusion limit, while still maintaining high spatial resolution, defined by the ultrasonic detection [12]. Photoacoustic computed tomography (PACT) is one implementation of PAT, where signals acquired from multiple detection positions are combined to reconstruct an image of the object [2]. To accelerate data acquisition, PACT usually uses a transducer array with hundreds of elements. So far, linear transducer arrays [30-32], circular transducer arrays [7, 8, 33] and arc transducer arrays [34] have all been used in PACT. Although circular transducer arrays can achieve full-view image quality, they are expensively custom-made, and their central frequencies are relatively low (less than 10 MHz) due to manufacturing constraints, which limit the spatial resolution for small-object imaging. In contrast, linear transducer arrays are commonly used in

18

ultrasonography. In particular, linear transducer arrays with high frequencies (central frequency >10 MHz) can be used to build high-resolution PACT. Moreover, linear transducer arrays can also be easily integrated with ultrasound imaging systems, leading to co-registered photoacoustic-ultrasonic imaging, which provides both optical and ultrasonic contrasts [31, 32, 35].

However, linear-array-based PACT suffers from limited view. Due to the limited detection aperture of the whole array and the limited receiving angle of each element, linear transducer arrays cannot capture photoacoustic (PA) waves over a full 360 degrees in a two-dimensional (2D) image plane. In fact, only boundaries that are nearly perpendicular to the acoustic axis of the linear transducer array can be detected. To increase the detection view for linear-array-based PACT, several methods have been developed. The most straightforward and easiest way is to circularly or semi-circularly scan either the linear transducer array or the imaging sample [36-38]. The time-consuming scan offsets the speed advantage of using a transducer array. Gateau et al. [39] proposed to use a ground glass diffuser to generate optical speckles as the illumination source, and by scanning the diffuser, they achieved full-view PACT images. However, this dynamic speckle method can image only shallow structures, and it still needs mechanical scanning. While an advanced algorithm [40] may be used to improve the imaging quality by removing streaking artifacts caused by the limited view, it cannot recover out-of-view boundaries. Ideally, we would like to enlarge the detection view of linear-array-based PACT without any mechanical scanning, in other words, without sacrificing the imaging speed. Acoustic reflectors redirect otherwise undetectable PA waves to the transducer array and hence increase the detection aperture [41]. Cox et al. [42] proposed to use two acoustic reflectors normal to the linear transducer array to get an infinitely wide virtual transducer array. However,

19

they demonstrate this full-view imaging capability only by numerical simulations, where each transducer element is assumed to be able to receive PA waves from all directions. In reality, the limited receiving angle of each transducer element would deteriorate the theoretical predictions. Huang et al. [43] experimentally proved that the detection view can be doubled by using a single 45-degree acoustic reflector adjacent to a linear transducer array. However, as the transducer array acceptance angle is typically less than 90 degrees, the doubled detection view from a single acoustic reflector is still insufficient to image more complex features. We need to further improve the detection view of a linear-array-based PACT. Moreover, Huang et al. utilized a low-frequency (5 MHz) linear transducer array, which is applicable to relatively large objects.

Methods   We propose a high-frequency linear-array-based PACT using two acoustic reflectors set at 120 degrees relative to each other. It is compared against a linear-array-based PACT both without and with a single 45-degree acoustic reflector, named "conventional PACT" and "single-reflector PACT", respectively.

Fig. 3.1(a) shows a schematic of the conventional PACT, which can collect only PA waves propagating towards the transducer array. The acceptance angle of each element is limited by the angular spread function, which is usually less than 60 degrees for high-frequency linear transducer arrays because of the relatively large ratio of the element width to the acoustic wavelength. Therefore, in Fig. 3.1(a) the horizontal boundary segments with detectable PA waves propagating along the –x direction can be reconstructed well, while the vertical boundary segments with undetectable PA waves propagating along the $\pm y$ direction cannot be reconstructed. To broaden the detection view, a 45-degree planar acoustic reflector was used to recover the vertical boundaries [43] [Fig. 3.1(b)]. With the aid of the acoustic reflector, the PA

waves propagating along the –*y* direction are redirected to the –*x* direction, and then received by the transducer array. While a single acoustic reflector can double the detection view, it is not enough to cover a full 360 degrees, even for large acceptance angle transducer elements. Naturally, one can add more reflectors to further extend the detection view and recover more boundaries. Fig. 3.1(c) shows acoustic reflectors set at an included angle of 120 degrees. Each reflector functions individually by redirecting the originally undetectable PA waves back to the transducer array elements, and together they recover more boundary features than a single reflector. In theory, two reflectors may cause multiple acoustic reflections between them. However, we did not observe obvious artifacts caused by multiple reflections in experiments, possibly due to reflection loss and acoustic attenuation, which rendered the multiple reflected signals negligible.

21
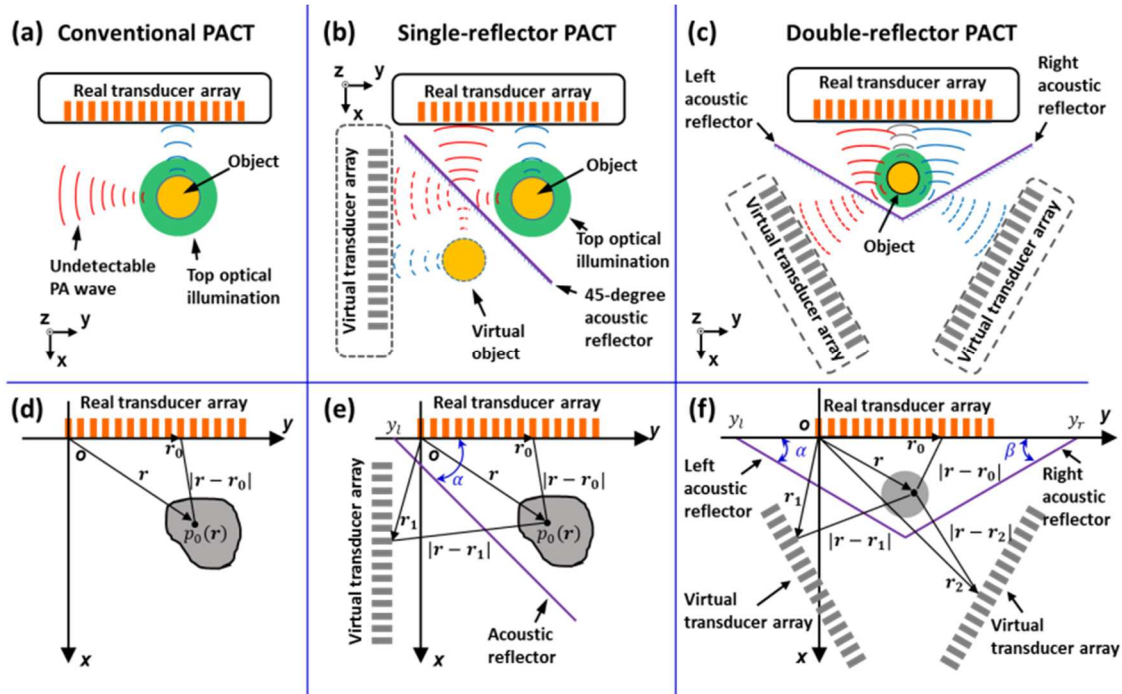
Figure 3.1 Schematics of the setups (a-c) and reconstruction processes (d-f) for conventional, single-reflector, and double-reflector linear-array-based PACT systems. $\mathbf{r_0}$, position of a real transducer element; $\mathbf{r_1}$ and $\mathbf{r_2}$, positions of virtual transducer elements; $\mathbf{r}$, position inside the object; p_0, initial PA pressure.

Images were reconstructed by using a filtered back-projection (FBP) algorithm [10]. Although it is not mathematically exact for the two-dimensional (2D) triangular measurement geometry, the FBP algorithm can be employed to generate boundary-enhanced images that accurately reveal the internal structures of the object. In future studies, advanced iterative image reconstruction methods [44, 45] can be employed with the reflector geometry to produce more quantitatively accurate images at the expense of image reconstruction speed. The image reconstruction geometries for conventional, single-reflector, and double-reflector PACT are illustrated in Figs. 3.1(d)-(e), respectively. In contrast to the conventional PACT image reconstruction, where transducer array data are used only once, single-reflector PACT image reconstruction duplicates the data from the real transducer array to the mirrored virtual transducer array; the acoustic reflector is removed, and the filtered back projection is performed in a boundary-free infinite medium [41, 43]. The virtual transducer elements $\mathbf{r_1}(x_1, y_1)$ are mirrored from the real transducer elements $\mathbf{r_0}(x_0, y_0)$ about the acoustic reflection plane. The reconstruction of the double-reflector PACT is similar to that of a single-reflector PACT, except that there is a third transducer array that is mirrored from the real transducer array about the right reflector. Strictly speaking, the filtered back projection assumes a constant speed of sound (SOS) within the imaging field. However, the SOS may vary within the sample and between the sample and the coupling medium. These effects are not considered in this study, as it has been demonstrated that a small SOS variation only slightly degrades the image quality [46].

We experimentally tested the single-reflector PACT and double-reflector PACT using the aforementioned reconstruction algorithm. A 532 nm wavelength laser illuminated the target from the $-z$ to $+z$ direction (top illumination), as shown in Fig. 3.1. The laser beam was generated from a second harmonic generator (OPOTEK Inc., Carlsbad, USA) pumped by a Nd:YAG laser (Brilliant, Quantel, Bozeman, USA) with 1064 nm output. This laser has a repetition rate of 20 Hz and an average pulse energy of 30 mJ. By using an engineering diffuser, the laser beam was expanded to a diameter of 1.6 cm on the top surface of the target, and therefore the laser fluence was 15 mJ/cm^2. A high-frequency linear transducer array with a central frequency of 15 MHz and a bandwidth of 9 MHz (MS200, Visualsonics Inc., Toronto, Canada) detected the PA waves. The MS200 linear transducer array has 256 elements, with a pitch of 125 μm and an effective detection aperture of 32.00 mm. The axial resolution (x-axis) in PACT was experimentally measured to be 113 μm, and the lateral resolution (y-axis) was 257 μm at a depth of 11 mm in water. The MS200 array also has a cylindrical acoustic lens with an elevational focal length of 18 mm and an elevational resolution of 1.2 mm in the elevational focal zone. The hypotenuse of an optical prism (PS911, Thorlabs Inc., Newton, USA) was used as the acoustic reflector for the single-reflector PACT. For double-reflector PACT, glass slides were used to reflect the PA waves. The prism and slides were made of BK7 glass, which has an acoustic impedance 10 times greater than that of the immersion liquid, and hence has a reflection coefficient close to unity. Although the amplitude and phase of the reflected acoustic wave change within the critical reflection angle of 26 degrees, here for simplicity we neglect this complexity and treat all reflections as total reflection without amplitude or phase change. As only a small amount of the signal comes from reflection within the critical angle, our assumption does not severely affect

the structural image quality. In future quantitative studies, we will develop a more rigorous algorithm to account for this effect.

In our study, both the direct and reflected PA waves were detected by the MS200 transducer array, which was connected to a commercial PA imaging system (Vevo LAZR, Visualsonics Inc., Toronto, Canada). The 256 signal channels were multiplexed to a 64-channel data acquisition system, resulting in an imaging speed of 5 Hz. The raw channel data were then transferred to a PC where the FBP algorithm was applied to reconstruct PACT images.
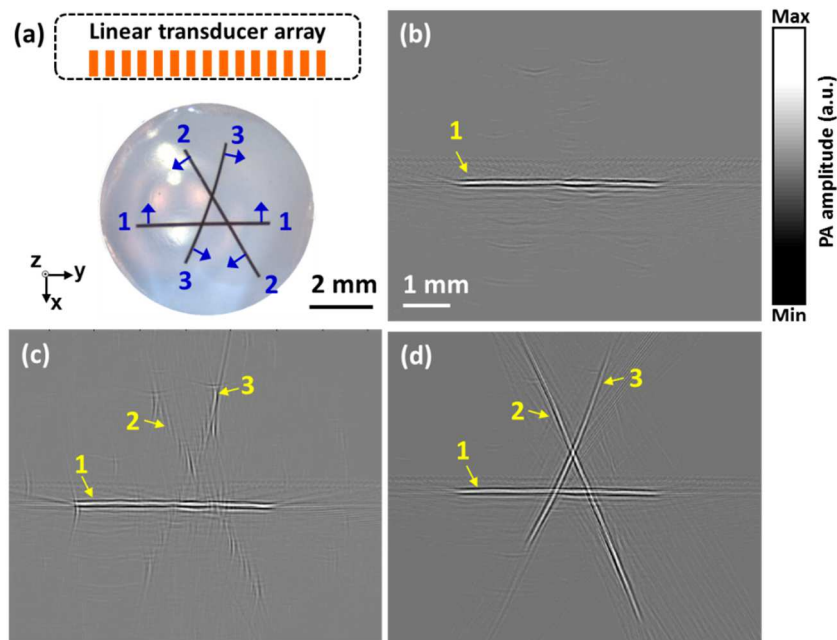
Figure 3.2 Simple phantom images. (a) Photograph of the crossed-hair phantom. PACT images acquired (b) without any acoustic reflector, (c) with one 45-degree planar acoustic reflector, and (d) with two ±120-degree planar acoustic reflectors.

Results   We first imaged a simple hair phantom as shown in Fig. 3.2(a). Three straight human hairs (labelled as "1-3") were embedded in a roughly triangular and planar arrangement in a 3% w/w agar gel. The generated PA waves propagated primarily along three directions at

24

120 degrees relative to each other, as indicated by blue arrows in Fig. 3.2(a). Fig. 3.2(b) is the reconstructed PA image acquired by the conventional PACT. The horizontal hair labelled as "1" was recovered, but hairs 2 and 3 were missed due to the limited view. Fig. 3.2(c) is the corresponding PA image acquired by the single-reflector PACT. While hair 1 was also reconstructed clearly, hairs 2 and 3 started to appear with obvious artifacts. Fig. 3.2(d) shows the corresponding PA image acquired by the double-reflector PACT, where all three hairs were recovered clearly.
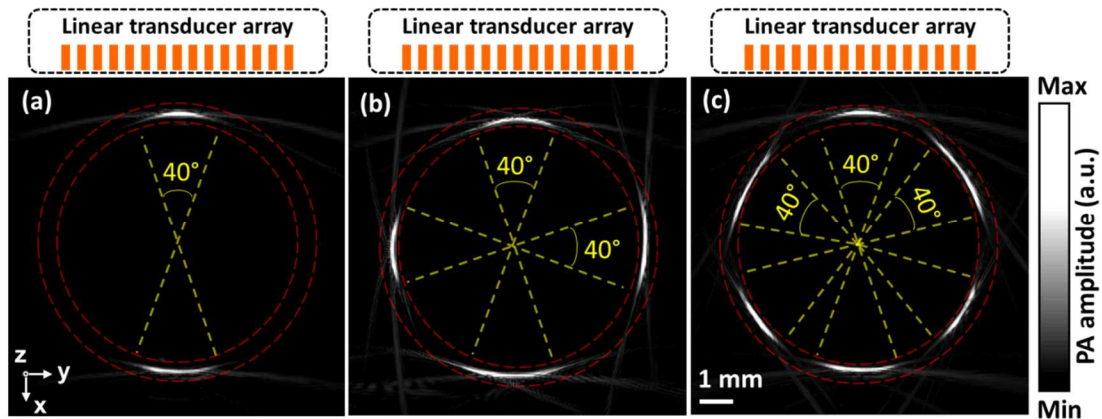
Figure 3.3 PACT images of a circular tube phantom acquired by (a) conventional PACT, (b) single-reflector PACT, and (c) double-reflector PACT. The view angle of the linear-array-based PACT doubles and triples with the single 45-degree planar acoustic reflector and two ±120-degree planar acoustic reflectors, respectively.

To quantitatively study the detection view enhancement, we imaged the cross-section of a tubular plastic drinking straw phantom in the x-y plane. The tube had an inner-diameter of 7.3 mm and a wall thickness of 0.15 mm. The circular tube generated PA waves in all 360 degrees in the 2D imaging plane, equivalent to the angular range from a point source at the center of the circle. Thereby we could quantitatively study the detection view of the three PACT systems. Fig. 3.3(a) shows the PA image of the circular tube acquired by the conventional PACT, where the

circle center was located at 11 mm away from the transducer surface. Both recovered top and bottom arcs have ~40 degrees of aperture with respect to the center, and this angle represents the receiving angle of the conventional PACT with respect to the circle center. Here the receiving angle is limited by two factors: the azimuth angle of the entire transducer aperture and the effective receiving angle of each individual transducer element. Because the azimuth aperture angle is ~55 degrees and the receiving angle of each transducer array element was experimentally measured to be ~40 degrees, the transducer element receiving angle is the limiting factor in this case. Fig. 3.3(b) shows the reconstructed circular tube phantom imaged with the single-reflector PACT system. Compared with Fig. 3.3(a), there are two more arcs, so the detection view of the linear-array-based PACT has increased from 80 degrees to 160 degrees, doubling the detection view of the conventional PACT system. Fig. 3.3(c) shows the same circular tube phantom image acquired by the double-reflector PACT system. It is obvious that the detection view has been triply increased, from 80 to 240 degrees.
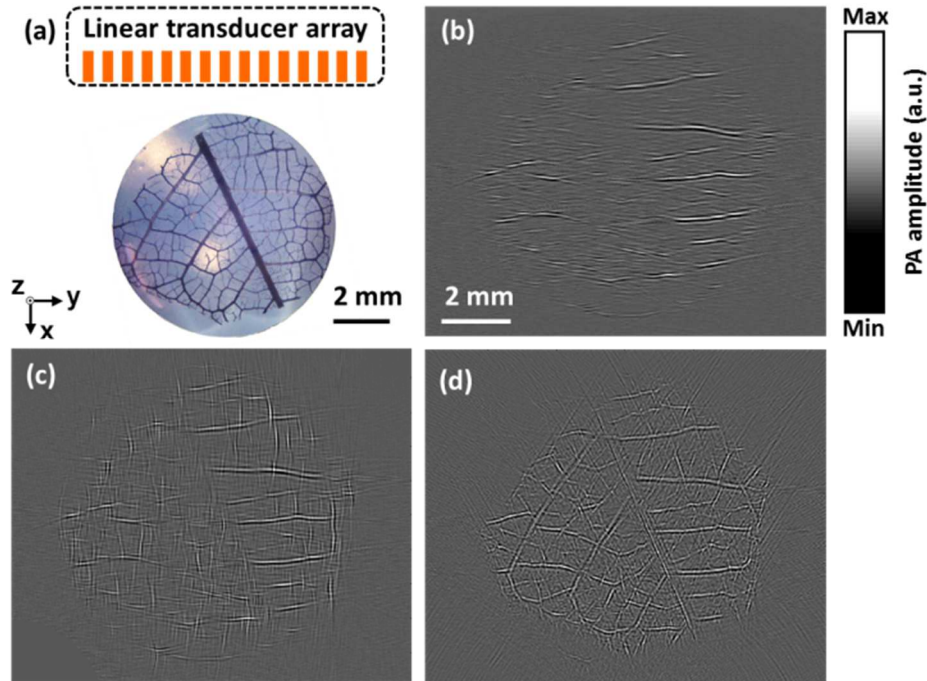
Figure 3.4 Leaf phantom images. (a) Photograph of the leaf phantom, (b) reconstructed PACT image without any acoustic reflector, (c) reconstructed PACT images with the 45-degree planar acoustic reflector, (d) reconstructed PACT images with two acoustic reflectors.

To verify the detection view enhancement, we imaged a complex phantom, a dehydrated leaf skeleton [Fig. 3.4(a)]. Compared with the hair phantom in Fig. 3.2(a), the leaf phantom has a rich vascular network and more complex features. Fig. 3.4(b) shows a reconstructed image of the leaf phantom with the conventional PACT. Only boundaries close to the horizontal direction were recovered. Fig. 3.4(c) shows an image of the phantom acquired by the single-reflector PACT. Some vertical boundaries were recovered, but there are still many unrecovered features. Fig. 3.4(d) shows a double-reflector PACT image, which recovers most of the features identifiable in the photograph in Fig. 3.4(a).

Discussion   We proposed a linear-array-based double-reflector PACT and compared it with conventional PACT without any acoustic reflector and with single-reflector PACT. In comparison to the conventional PACT, double-reflector PACT triples the original detection view, while still keeping the original imaging speed. Although the double-reflector PACT still has not achieved 360-degree (i.e., full-view) detection due to the limited receiving angle of the single transducer element, it will be possible to achieve a full view in the future by using linear transducer arrays with larger element receiving angles and wider apertures.

3.2   Augmenting the Detection View Angle Using Ultrasonic Thermal Encoding

Background The photoacoustic (PA) effect describes the generation of acoustic waves due to time-variant photon absorption and thermoelastic expansion. As optical absorbers are excited almost simultaneously, PA waves tend to propagate along directions normal to the boundaries of

the absorbing structure [41, 47, 48]. To capture all the features of arbitrarily shaped objects, full-view ring or spherically shaped ultrasonic detection arrays have been used to cover all the PA propagation directions in two dimensions (2D) or three dimensions (3D). However, these transducers are usually custom-made, expensive, and have closed working spaces, limiting their applications to targets such as small animals, human fingers or breasts [34, 49, 50].

In order to image more anatomical sites, such as the liver, kidney, or brain of humans and large animals, ultrasonic transducers with one-sided accessibility, such as single-element focused transducers or linear transducer arrays, are often preferred [51-54]. However, these types of transducers suffer limited views, which must be addressed in order to avoid missing important features, such as vessels or tumor margins [43, 55]. A possible solution is to generate non-uniform PA emissions, so that the PA waves propagate in all directions. A novel approach based on optical speckle illumination has been utilized to induce such non-uniformity [39]. Because each optical speckle grain can be treated as a PA source, the PA emission angle is enlarged. A limitation in deep tissue is that the speckle grains may be small and densely distributed within the acoustic focus, which decreases the signal strength.

Here we present a different approach to virtually augment the PA detection view angle using ultrasonic thermal encoding, which is analogous to a method in microwave thermal imaging [56]. A focused ultrasonic transducer thermally encodes a voxel. Due to the temperature dependence of the Grueneisen parameter [57-61], the encoded voxel emits stronger PA waves than other voxels. The amplitude-increased PA waves propagate in all directions because of the round cross section of the heating spot. By scanning the thermally encoded spot, a full-view PA image can be formed despite the use of a limited-view PA detector.

Principle   Under stress and thermal confinements, a short-pulsed laser beam illuminating an optically absorbing object generates an initial pressure rise p_0:

$$p_0(\vec{\rho}) = \Gamma_0(\vec{\rho})\eta\mu_a(\vec{\rho})F(\vec{\rho}) \quad (3.1)$$

where $\vec{\rho}$ is a vector representing an arbitrary point, Γ_0 is the Grueneisen parameter at the baseline temperature, η is the percentage of the optical absorption that is converted into heat, μ_a is the optical absorption coefficient, and F is the local optical fluence. Here, we assume that the heat conversion efficiency η is spatially invariant.

The Grueneisen parameters for many materials, such as water, aqueous solutions, and many biological tissues, are temperature dependent. With a small temperature rise ΔT, the Grueneisen parameter Γ can be approximated using the first-order Taylor expansion as

$$\Gamma(\vec{\rho}, \Delta T) = \Gamma_0(\vec{\rho}) + \Gamma'_0(\vec{\rho})\Delta T(\vec{\rho}) \quad (3.2)$$

where Γ'_0 is the temperature derivative of Γ at the baseline temperature.

With ultrasonic heating, the initial pressure rise $p_0^{th}(\vec{\rho})$ becomes

$$p_0^{th}(\vec{\rho}) = \Gamma_0(\vec{\rho})\eta\mu_a(\vec{\rho})F(\vec{\rho}) + \Gamma'_0(\vec{\rho})\Delta T(\vec{\rho})\eta\mu_a(\vec{\rho})F(\vec{\rho}) \quad (3.3)$$

On the right hand side of Eq. 3.3, the first term represents the original initial pressure rise, and the second term is the initial pressure rise due to the temperature rise. The acoustic pressure $p^{th}(\vec{\rho}, t)$ propagation in an inviscid medium can be described as [62]

$$p^{th}(\vec{\rho},t) = \frac{\Gamma_0(\vec{\rho})\eta F(\vec{\rho})}{4\pi v_s^2} \frac{\partial}{\partial t} \left[\frac{1}{v_s t} \int \mu_a(\vec{\rho}')\delta\left(t - \frac{|\vec{\rho}-\vec{\rho}'|}{v_s}\right)d\vec{\rho}' \right]$$

$$+ \frac{\Gamma'_0(\vec{\rho})\eta F(\vec{\rho})}{4\pi v_s^2} \frac{\partial}{\partial t} \left[\frac{1}{v_s t} \int \Delta T(\vec{\rho}')\mu_a(\vec{\rho}')\delta\left(t - \frac{|\vec{\rho}-\vec{\rho}'|}{v_s}\right)d\vec{\rho}' \right] \qquad (3.4)$$

where v_s is the speed of sound, and $\delta(\cdot)$ is the Dirac delta function. The first term on the right

hand side of Eq. 3.4 represents the original PA waves, whose propagation direction is determined

by the absorber distribution $\mu_a(\vec{\rho})$. The second term is generated from the augmented

Grueneisen parameter, whose propagation direction is determined by product of the optical

absorption distribution and the ultrasonic heating, i.e., $\Delta T(\vec{\rho})\mu_a(\vec{\rho})$. Therefore, we can apply

ultrasonic heating patterns $\Delta T(\vec{\rho})$ to manipulate the propagation directions of the augmented

PA waves, so that they can be received by the PA detector.

Let us consider a simplified example: a long cylindrical object uniformly illuminated by omni-

directionally scattered light. Using the cylindrical coordinates z and r (i.e., $r = (x^2 + y^2)^{1/2}$), the

absorption coefficient can be written as

$$\mu_a(r) = \mu_{a0}U(R-r) \quad (3.5)$$

where R is the radius of the cylindrical object, and U is the Heaviside step function defined as

$$U(m) = \begin{cases} 1 & for \quad m \geq 0 \\ 0 & for \quad m < 0 \end{cases} \qquad (3.6)$$

If the object is optically thin, i.e., $\mu_{a0}R \Box 1$, the optical energy will be uniformly deposited

within the cylinder. In this case, by substituting Eq. 3.5 into Eq. 3.4, we can write the PA

pressure as [63]

$$p_c(\tau) = \frac{\Gamma_0 \eta \mu_{a0} F}{\pi (2r)^{0.5}} \int_{-\chi}^{0} \frac{\xi + 1}{(\xi + \tau)^{0.5} \left[1 - (\xi + 1)^2\right]^{0.5}} d\xi \quad (3.7)$$

where τ is the dimensionless retarded time from the edge of the cylinder, defined as

$\tau = \left(\frac{v_s}{R}\right)\left[t - \frac{(r - R)}{v_s}\right]$, and χ is the lesser of 2 or τ. Here $p_c(\tau)$ represents a cylindrical PA wave,

which propagates along only the radial direction, not the *z*-axis (not considering the ends of the

cylinder). Hence, the limited-view problem appears when an ultrasonic transducer cannot receive

the cylinder's pressure wave in the radial direction.

After applying a spherical ultrasonic heating pattern with a radius R' (let $R' \leq R$) to the long

cylinder, we generate an additional spherical PA source due to the changed Grueneisen

parameter. The new PA wave generated by the heated cylindrical object can be written as [63]

$$p(\tau, \tau') = p_c(\tau) + p_s(\tau') =$$
$$p_c(\tau) + \frac{\Gamma_0' \Delta T \eta \mu_{a0} F}{2\rho}(1 - \tau')\left[\Theta_{0,1}(\tau') + \Theta_{1,2}(\tau')\right] \quad (3.8)$$

where τ' is the dimensionless retarded time from the edge of the sphere, defined as

$\tau' = \left(\frac{v_s}{R'}\right)\left[t - \frac{(l - R')}{v_s}\right]$, $l = \sqrt{r^2 + z^2}$ is the radial distance in a spherical coordinate, and $\Theta_{i,j}(\cdot)$ is

a square wave function defined as $\Theta_{i,j}(m) = \begin{cases} 1 & \text{for } i \leq m \leq j \\ 0 & \text{else} \end{cases}$. Eq. 3.8 indicates that the

ultrasonic heating generates an additional spherical PA wave that can be detected at any view

angle.

Similarly, line-shaped ultrasonic heating patterns can also be used to manipulate the propagation direction of the PA waves. In this case, the normal direction of the heating line should be within the receiving angle of the ultrasonic transducer, and the distance between the lines should be greater than the ultrasonic resolution.

Numerical Simulation   Numerical simulation was carried out to validate the full-view imaging capability offered by thermal encoding. We used the k-Wave toolbox [64, 65] for fast numerical simulation of PA wave propagation. Images were reconstructed with the time-reversal algorithm in the k-Wave toolbox. The simulation geometry is shown in Fig. 3.5 (a). A linear ultrasonic array was positioned orthogonally to a line-shaped numerical phantom. The linear transducer array has 200 elements, with a pitch of 0.1 mm and a 15 MHz bandwidth. The simulation was performed in a 2D plane with a field of view (FOV) of 20×20 mm^2 and a pixel size of 0.1×0.1 mm^2. To mimic the thermal encoding, we increased the initial pressure rise at the heated point. The simulation code can be found in supplemental materials.
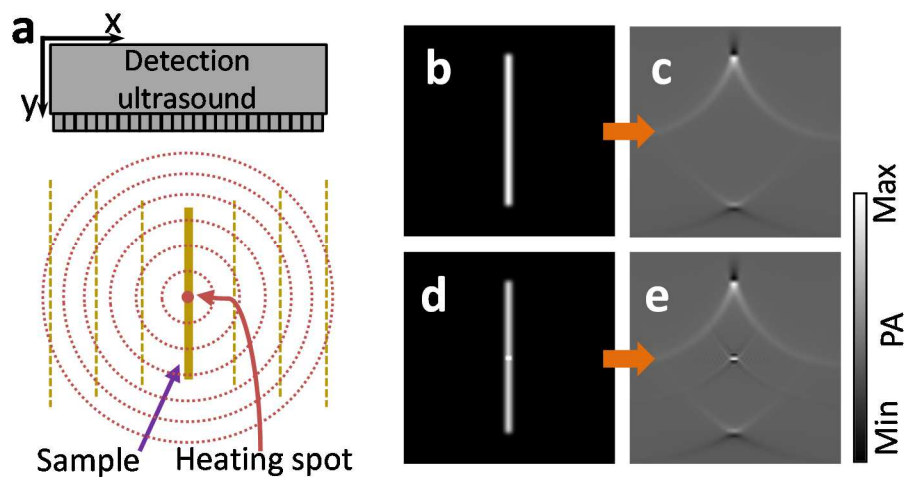
Figure 3.5 Numerical simulation of the virtually enabled full-view PA imaging using ultrasonic thermal encoding. (a) Schematic of the simulated imaging setup. The heating ultrasonic transducer is not shown. (b-e) Simulations of a vertical line object without and with point ultrasonic heating. (b) Initial pressure rise of the line object without ultrasonic heating. (c) Reconstructed PA image of the line object without ultrasonic heating. (d) Initial pressure rise

32

of the line object with an ultrasonic heating spot. (e) Reconstructed PA image of the overlap between the ultrasonic heating spot and the line object.

Figs. 3.5 (b-e) present the numerical simulation of a line object without and with point ultrasonic heating. Fig. 3.5 (b) shows the initial pressure rise without ultrasonic heating. Since the initial pressure rise on the line phantom was uniform, the PA waves propagated only along the two normal directions of the line (except at the two ends of the line object). Because the ultrasonic transducer array received PA signals only from the two ends, the reconstructed PA image in Fig. 3.5 (c) does not show the middle part of the line object. When the simulated ultrasonic heating was on, the heated spot generated higher initial pressure rise, as shown in Fig. 3.5 (d). While the baseline PA wave still propagated normal to the line object's boundaries, the incremental PA wave from the heated spot propagated along all directions and was received by the linear transducer array. The reconstructed image in Fig. 3.5 (e) demonstrates that the heated spot in the line phantom could be detected by the limited view ultrasonic transducer array.

From the simulation results, we can find that the thermal encoding method successfully recovers the originally "invisible" point. Combined with raster scan, it can recover a full-view photoacoustic image.
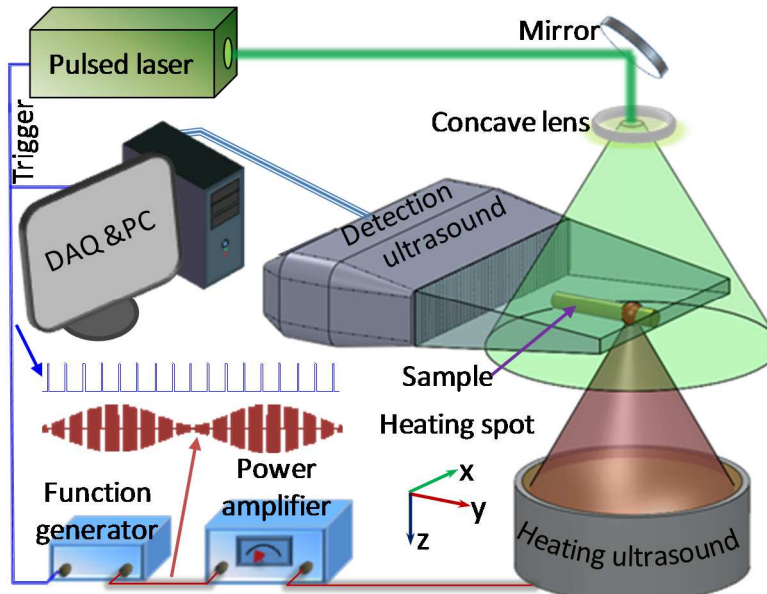
Figure 3.6 Schematic of a full-view photoacoustic imaging system based on acoustic thermal tagging.

Experimental Setup The experimental setup is illustrated in Fig. 3.6. A pulsed laser (Nd:YAG, Quantel; 532-nm wavelength; 10-ns pulse duration; 20-Hz pulse repetition rate) provided optical excitations. The output laser beam was expanded by a concave lens to illuminate the sample. A 256-element linear ultrasonic transducer array (MS200, Visualsonics Inc., Canada, 15-MHz central frequency, 9-MHz one-way bandwidth quantified as the full width at half maximum or FWHM) was used to detect the PA waves. The ultrasonic array was connected to a PA imaging system (Vevo LAZR, Visualsonics Inc., Canada), which could form a two-dimensional PA image using four laser pulses. The measured lateral (x-axis) resolution was 257 μm when the sample was positioned ~11 mm away from the transducer surface, and the measured axial (y-axis) resolution was 113 μm.

A custom-made ultrasonic heating transducer was employed for thermal encoding. The transducer had a resonant frequency of 7.5 MHz, an estimated FWHM focal diameter of 178 μm,

34

and an estimated FWHM focal depth of 445 μm. The parameters of the heating transducer array were selected to generate a focal spot size smaller than the lateral resolution of the linear transducer array for isotropic detection. The heating beam was placed vertically and focused onto the PA imaging plane. A function generator synthesized a 7.5 MHz sinusoidal signal, whose amplitude was modulated by another sinusoidal wave at a frequency of 0.5 Hz. The modulated 7.5 MHz sinusoidal signal was amplified to drive the heating ultrasonic transducer. To avoid interference between the acoustic heating and PA detection, the heating ultrasound was turned off for one millisecond before and after each PA acquisition. At each heating spot, 50 consecutive 2D PA images were acquired at a speed of 5 images per second and reconstructed using the filtered backprojection algorithm [10]. The intensities of each pixel in the 50 2D images were transformed into the frequency domain, where the 0.5-Hz frequency component of every pixel was used to form an intermediate PA image. The focus of the heating ultrasonic transducer was raster scanned with a step size of 250 μm over the *x-y* plane. The step size was chosen to be close to the value of the lateral resolution to ensure the spatial fidelity while maximally reducing the scanning time. All the intermediate PA images were combined to synthesize a final PA image. Each pixel value of the synthesized PA image is determined from the maximum value from the corresponding pixels in all the intermediate PA images.

The thermal encoding effect was first tested by imaging bovine blood flowing in a silicone tube (0.5-mm inner diameter, and 1-mm outer diameter) placed along the *x* axis. The heating spot was placed at the center of the tube. To avoid possible heat accumulation, the blood was pumped to flow in the tube at a speed of ~5 mm/sec. The heating power was modulated at 0.5 Hz, with an average power of 1 W. The average power was calculated from the sinusoidal peak powers, which were read from the radio-frequency amplifier.
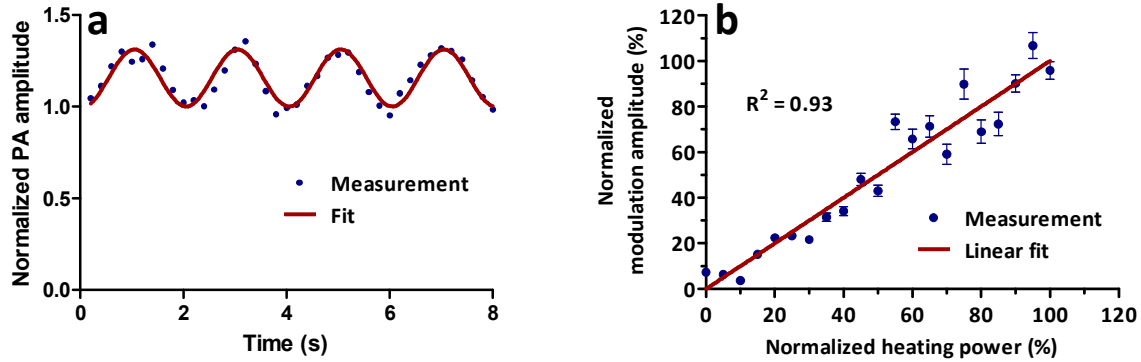
Figure 3.7 Ultrasonic thermal encoding test. (a) PA amplitude change with 0.5-Hz modulated ultrasonic heating; (b) PA modulation amplitude versus ultrasonic heating power. Error bars represent standard errors. N = 8.

Results Fig. 3.7 (a) shows the measured PA signal amplitude varying at 0.5 Hz, following the heating power modulation. In another test, the average heating power was increased from 0 to 1 W. The PA modulation amplitudes were recorded at each power level, and are plotted in Fig. 3.7 (b). The PA modulation amplitude is proportional to the average heating power, which again validates the linear assumption. There is a trade-off between the heating spot size and the heat loss rate due to thermal diffusion, which determines the choice of the heating ultrasonic transducer.

Next, a vertical (i.e., along the *y* axis) blood tube phantom was imaged to validate the augmented detection view. The experimental results are presented in the supplementary materials. Finally, as a validation of the concept, the vasculature in a mouse ear was imaged *in vivo* without and with ultrasonic thermal encoding. The mouse ear was mounted in the PA imaging plane. We first acquired a regular PA image without ultrasonic thermal encoding. As shown in Fig. 3.8 (a), although the PA image has a decent SNR, it shows only horizontal or nearly horizontal blood vessels. Many vertical features are missing. Then we applied ultrasonic thermal encoding and acquired PA images of the same region. The synthesized PA image is shown in Fig. 3.8 (b),

where blood vessels along all directions are visible. To facilitate comparison, Fig. 3.8 (c) presents an overlaid version of both images. This comparison shows the *in vivo* full-view imaging capability, even using a limited-view PA detector.
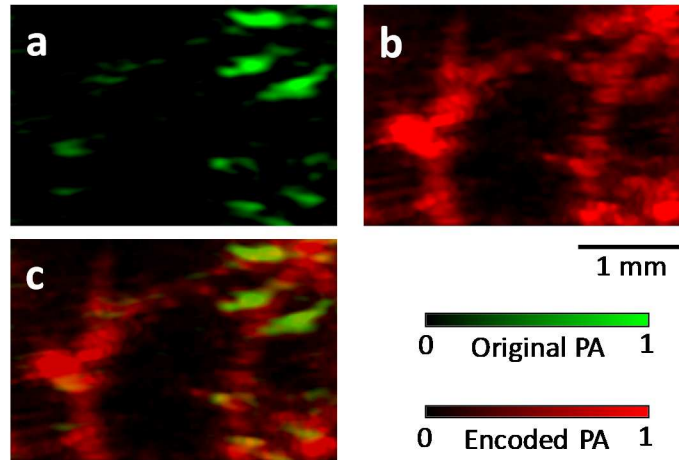
Figure 3.8 (a) *In vivo* mouse vascular imaging without ultrasonic thermal encoding. Only horizontal or nearly horizontal blood vessel segments are visible. (b) *In vivo* vascular imaging with ultrasonic thermal encoding. More blood vessels are visible due to the enlarged view angle. (c) Overlay image showing co-registered original and thermally encoded PA images.

In the present experimental setup, the heating transducer and the PA detection transducer are deployed orthogonally. Rotating the sample by 45 degrees may allow accessing a large sample on one side. If the heating transducer has to be placed co-axially with the detection transducer, a high-NA heating transducer will be needed to make the heating voxel nearly spherical.

The images acquired with ultrasonic thermal encoding are sensitive not only to optical absorption, but also are affected by the acoustic absorption and the Grueneisen parameter's first-order derivative with temperature.

To address the concern of tissue damage from ultrasonic heating, the maximum temperature rise was estimated from the PA amplitude increase. According to the results in Fig. 3.7, the PA signal change was an appropriate indicator of temperature rise. In the phantom experiments, the

maximum PA amplitude increase was 29±2%. Assuming that the Grueneisen parameter is proportional to temperature in degrees Celsius [66] and the baseline temperature is 20°C, the maximum temperature rise was estimated to be ~5.8°C. For the *in vivo* imaging, the baseline temperature was body temperature (37°C) and the maximum PA amplitude increase was ~12±3%. These values indicate a temperature rise of ~4.4°C. Considering that blood flow can dissipate heat efficiently, the moderate local ultrasonic heating does not likely cause thermal damage to biological tissue. Moreover, if we can improve the PA detection sensitivity, the temperature rise can be further reduced. Another limitation is that during thermal encoding heat may dissipate to neighboring tissues, which can lower the encoding efficiency. Shortening the thermal encoding time may mitigate this effect.

In this work, single-spot ultrasonic heating was raster scanned to generate a 2D image, which is time-consuming. For example, the *in vivo* mouse ear vascular image in Fig. 3.8 (b) has a field of view of 5×5 mm^2 with 400 heating spots. At each heating spot, we acquired 50 frames of PA images at a speed of 5 frames per second (10 seconds per heating spot). Thus, it took 66 minutes to acquire the image. Because the main purpose of this paper is to demonstrate the principle, the imaging speed is not optimized here. In the future, faster PA imaging systems and shorter heating time can be used to improve the imaging speed. At each spot, the heating time should be long enough to allow heat exchange, which might limit the ultimate imaging speed. In addition, complex structured ultrasonic heating patterns, such as multiple spots, a single line, or even multiple lines, can be applied to simultaneously encode multiple features. These patterns can potentially be generated by either a cylindrically focused ultrasonic transducer or a 2D ultrasonic transducer array.

Discussion The thermal encoding in this work can potentially be implemented on a high-intensity focused ultrasound (HIFU) treatment system in the future to provide PA imaging capability during treatment. Since some HIFU setups have dynamic focusing capability in both depth and lateral direction, it becomes possible to achieve an electronic thermal encoding scan, instead of a mechanical scan [67].

3.3 Conclusions

Linear-array PACT suffers from limited view. By using two acoustic reflectors, we tripled the detection view angle of a linear-array-based PACT system, from 80 to 240 degrees, while maintaining the imaging speed. We introduced virtual transducer arrays into the image reconstruction plane to remove the boundaries created by reflectors, and then we applied the filtered backprojection algorithm for image reconstruction. Imaging a complex phantom demonstrated the enlarged detection view angle of the double-reflector method. Double-reflector reflector PACT may prove valuable in biomedical imaging studies where both high image quality and high imaging speed are desired.

We also present a new approach using ultrasonic thermal encoding to solve the limited-view problem. The ultrasonic thermal encoding was modeled and experimentally validated. Full-view PA imaging capability was demonstrated both in phantoms and *in vivo*, even using a limited-view PA detector. Since ultrasonic heating can be focused deeply, this method can be applied to deep tissue. The improved view angle dramatically enhanced the PA imaging of arbitrarily oriented blood vessels. The improved technique is promising for full view imaging of other features of biomedical interest, such as tumor margins.

Chapter 4: Multi-view Linear-array Photoacoustic Computed Tomography

This chapter describes technical developments in linear-array PACT with multi-view scanning. Multi-view Hilbert transformation allows us to get accurate optical absorption, and the linear-rotational linear-array PACT improves the spatial resolution significantly. Part of this chapter has been published in the Journal of Biomedical Optics[68].

4.1 Multi-view Hilbert Transformation for Full-view Linear-array PACT

Background Photoacoustic computed tomography (PACT) is an incarnation of photoacoustic tomography (PAT) that provides optical contrast information in deep biological tissues [2]. Unlike focused-scanning photoacoustic microscopy (PAM), which forms images by combining A-lines, PACT forms images through reconstruction algorithms. To accelerate imaging speed, PACT is usually implemented with an ultrasonic transducer array employing 64-512 elements to detect photoacoustic (PA) signals in parallel. Currently, both curved and linear transducer arrays are widely used in PACT. Although curved transducer arrays, such as full-ring transducer arrays [7, 8, 69] and partial-ring transducer arrays [34, 70], have greater detection view coverage [47], they are custom-designed, costly, and offer few frequency choices. In contrast, linear transducer arrays have the advantages of low cost, wide bandwidth selection, hand-held operation, and ultrasonic imaging integration. Although linear-array PACT suffers from the limited-view problem, rotating either the transducer array or the imaging objects circularly enables full-view linear-array PACT, at the expense of longer imaging time [36-38, 71, 72].

Challenges still remain in full-view linear-array PACT. First, no full-view linear-array PACT has been reported with a central ultrasonic frequency higher than 24 MHz, which limits the spatial

resolution. A higher central frequency would provide finer lateral resolution, and the associated wider bandwidth would result in higher axial resolution, allowing imaging of finer structures in biological tissues, at the expense of penetration. Second, due to the band-pass frequency response of the transducer elements, the reconstructed images present bipolar (i.e., both positive and negative) pixel values unless the raw channel data is deconvolved with the system's electrical impulse response (EIR) and non-negativity is enforced. Because PACT should ideally image the initial pressure or optical energy deposition, which is always non-negative, bipolar pixel values are artificial. It is also counterintuitive for physicians and biologists to interpret the images because both positive and negative peaks represent strong optical absorption. Moreover, bipolar pixel values are not conducive to quantification of physiological parameters, such as oxygen saturation (sO_2) and blood flow speed.

Thus far, three solutions have been proposed. The first solution is to simply threshold negative signals to zero [38, 71, 72]. However, thresholding removes structures from the image and introduces image artifacts. The second solution is to deconvolve the raw channel data with the EIR. However, this method requires a high signal-to-noise ratio (SNR) and accurate measurement of each element's EIR. The third solution is to iteratively reconstruct an image with the non-negativity constraint [44, 45]. However, this method requires both accurate modeling of the whole imaging system and time-consuming computation. Thus, there is an urgent need for a simple and effective method to make bipolar pixel values unipolar.

Hilbert transformation along the acoustic axis recovers the envelope without knowledge of the EIR. Therefore single-view Hilbert transformation has been widely applied in computing the A-lines of a PAM image and beamformed A-lines of a single-view linear-array PACT image, along the acoustic axis. However, single-view Hilbert transformation cannot be applied directly to full-

41

view linear-array PACT because the full-view linear-array PACT has different acoustic axis directions. Hilbert transformation along a single direction will cause artifacts due to the mismatch between the Hilbert transformation direction and acoustic axis. Therefore we propose a novel multi-view Hilbert transformation method that solves this problem by coherently reconstructing bipolar images in each view, then applying Hilbert transformation along each view's acoustic axis and taking the absolute value to recover the envelope, and finally adding unipolar single-view envelope images together to form a full-view unipolar image. This algorithm has never been reported previously.

Methods   We present a high-frequency full-view linear-array PACT imaging system, as shown in Fig. 4.1(a). The illumination source was a 532 nm wavelength laser beam from a second harmonic generator, which was pumped by a Nd:YAG 1064 nm wavelength laser (Brilliant B, Quantel Inc.) at a repetition rate of 20 Hz. The laser beam was expanded by a circle-pattern engineered diffuser (EDC-5-A-2s, RPC Photonics Inc.) to a diameter of 20 mm on the object's surface. With a total energy of 35 mJ per laser pulse, the optical fluence on the object's surface was estimated to be 11 mJ/cm^2, well below the ANSI safety limit (20 mJ/cm^2). The excited PA waves were received by a linear transducer array (MS550D, Visualsonics Inc.) with 256 elements and an element-to-element pitch of 55 μm. Each element had a central frequency of 40 MHz and a bandwidth of 33 MHz. The MS550D transducer was connected to an ultrasound/photoacoustic (US/PA) dual modality imaging platform (Vevo LAZR, Visualsonics Inc.), where co-registered US/PA images were acquired and displayed. During experiments, the object to be imaged, either a zebrafish, leaf skeleton, or black microsphere, was fixed on a manual rotation stage (K6X, Thorlabs Inc.) and immersed in water. To get a two-dimensional (2D) full-view linear-array PACT image, samples were rotated, and images were acquired at

42

multiple angles. After imaging, raw data acquired at all view angles were exported from the Vevo LAZR imaging platform to a computer.
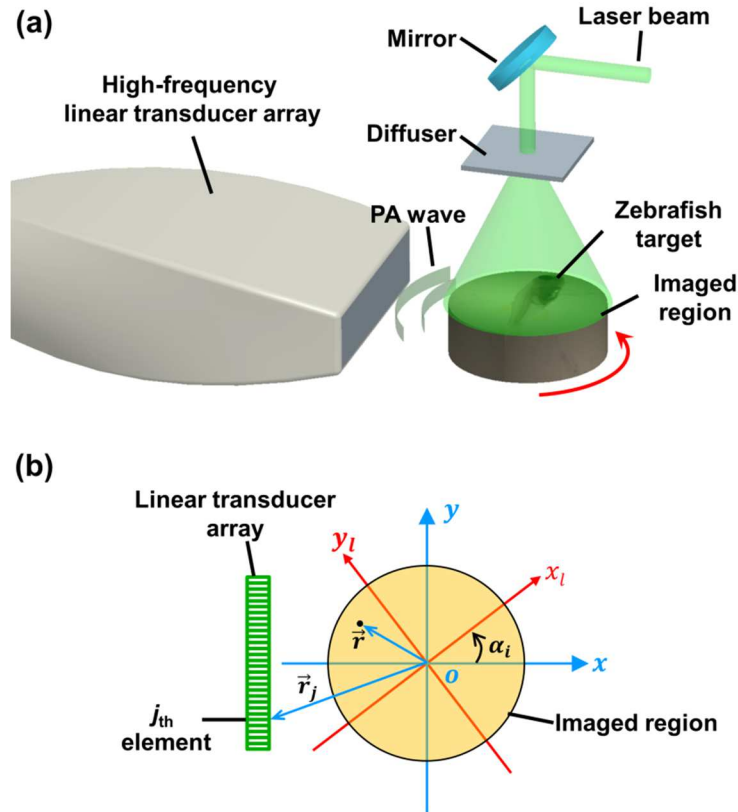
Figure 4.1 (a) Setup of the high-frequency full-view linear-array PACT system. (b) Schematic of the scan process. PA: photoacoustic. The local coordinates are aligned with the global coordinates when the object is imaged at the first view angle (i.e., $\alpha_i = 0$).

A schematic diagram of the reconstruction process is shown in Fig. 4.1(b), where two coordinate systems are used: the global coordinates $\vec{r} = (x, y)$ attached to the fixed linear transducer array, and the local coordinates $\vec{r}_l = (x_l, y_l)$ attached to the sample to be rotated. Both coordinates share the same origin, but the local coordinates rotate with the sample while the global coordinates are fixed. At rotation step i, the single-view PACT image is reconstructed under the global coordinates using the universal filtered back-projection (FBP) algorithm [10]:

$$p_0^{(i)}(\vec{r}) = \int_{\Omega_0} \frac{d\Omega_0}{\Omega_0} \left[2p(\vec{r}',t) - 2t \frac{\partial p(\vec{r}',t)}{\partial t} \right]_{t=\frac{|\vec{r}-\vec{r}'|}{c}}$$

where $p(\vec{r}',t)$ is the acoustic pressure measured by the transducer element located at $\vec{r}'$ and time t. $p_0^{(i)}(\vec{r})$ is the reconstructed initial PA pressure for the point at $\vec{r}$. As mentioned previously, due to the limited view and finite bandwidth of the transducer, the reconstructed $p_0^{(i)}(\vec{r})$ is bipolar. c is the speed of sound and is assumed to be uniform. Ω_0 is the solid angle subtended by the detection aperture of the transducer array with respect to the point $\vec{r}$, and $d\Omega_0/\Omega_0$ represents the weighting factor of the contribution of the transducer element located at $\vec{r}'$. Although the FBP is not a mathematically exact algorithm for the 2D reconstruction, it can generate boundary-enhanced images that accurately reveal the internal structures of the object. In the future, a more accurate 2D reconstruction algorithm may be applied.

With the assumption that the light illumination is rotationally symmetric, a full-view bipolar PACT image can be formed in the local coordinates by rotating the reconstructed images acquired at all angles from the global coordinates to the local coordinates, then averaging:

$$p_0(\vec{r_l}) = \frac{1}{N}\sum_{i=1}^{N} \boldsymbol{R}_{-\alpha_i}\left\{ p_0^{(i)}(\vec{r}) \right\}. \qquad (2)$$

Here, $\vec{r_l}$ is the image point in the local coordinates, $p_0(\vec{r_l})$ is the reconstructed full-view bipolar PACT image, N is the total number of rotation steps (views), $\boldsymbol{R}$ is the rotation operator that transforms an image in the global coordinates $\vec{r}$ to an image in the local coordinates $\vec{r_l}$, and $\alpha_i = (i-1)2\pi/N$ is the rotation angle for the i-th step.

To reconstruct the full-view unipolar image, we propose a four-step reconstruction procedure:

Step 1: At each rotation angle α_i, reconstruct the bipolar PACT image in the global coordinates (x, y), using the universal FBP algorithm.

Step 2: For each bipolar image from step 1, take Hilbert transformation along the depth direction $(+x)$ and calculate the amplitude by taking the absolute value.

Step 3: Rotate the processed image from step 2 by an angle of $-\alpha_i$, transforming it from the global coordinates (x, y) to the local coordinates (x_l, y_l).

Step 4: Repeat steps 1-3 for all rotation angles, and average pixel by pixel over all the images.

Mathematically, this process can be formulated as

$$p_0^+(\vec{r}_l) = \frac{1}{N}\sum_{i=1}^{N} R_{-\alpha_i}\left\{A\left\{H\left\{p_0^{(i)}(\vec{r})\right\}\right\}\right\}, \qquad (3)$$

where, $p_0^+(\vec{r}_l)$ is the final unipolar image, A is the absolute value operator, and H is the Hilbert transformation operator. Note that Eq. (3) represents a non-linear process because of the amplitude extraction, while the conventional FBP algorithm is linear.

Results　　　We imaged a dehydrated leaf skeleton to demonstrate the full-view linear-array PACT. The leaf skeleton was sealed in a 3% agar gel. Fig. 4.2(a) shows the setup of the single-view linear-array PACT, and Figs. 4.2(b) and 4.2(c) show a single-view bipolar image and a unipolar image, respectively. Due to the limited view of single-view linear-array PACT, only features with surface normals aligned to the acoustic axis can be reconstructed [47]. Fig. 4.2(d) shows the setup for acquiring six views with an angular step size of 30 degrees, and Figs. 4.2(e) and 4.2(f) show the corresponding bipolar image and unipolar image of the leaf skeleton,
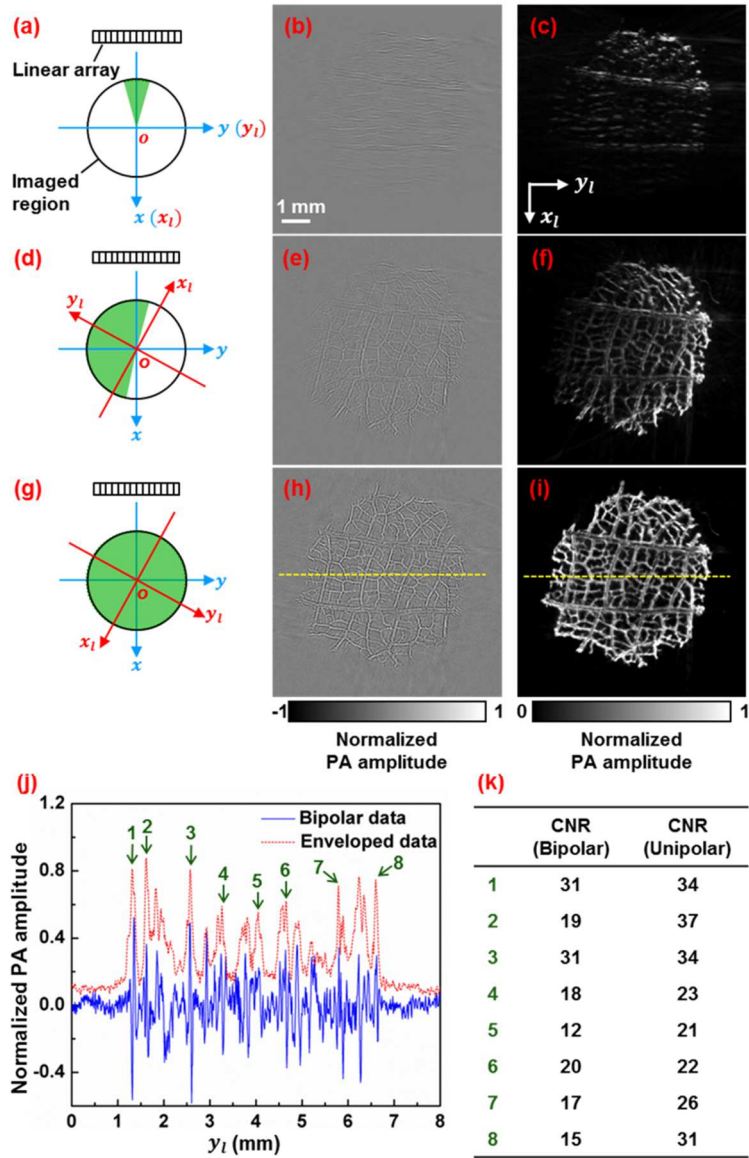
Figure 4.2 (a) Single-view linear-array PACT setup with acquired (b) bipolar image and (c) unipolar image. (d) Six-view linear-array PACT setup with acquired (e) bipolar image and (f) unipolar image. The green area indicates the photoacoustic detection angle coverage. (g) Full-view linear-array PACT setup with acquired (h) bipolar image and (i) unipolar image. (j) Comparison of the full-view bipolar and unipolar image profiles along the dashed lines in (f) and (i). (k) CNR (contrast-to-noise ratio) comparison of selected features in bipolar and unipolar profiles as marked in (j).

respectively. Compared with the single-view images, multi-view images clearly recovered more features. Fig. 4.2(g) shows the full-view PACT setup with 12 views and an angular step size of

30 degrees. Figs. 4.2(h) and 4.2(i) show a full-view bipolar image and unipolar image of the leaf skeleton, respectively. Compared with the six-view images, full-view images revealed even more features. We can see that more features of the leaf are gradually revealed as the number of views increases.

Comparing the full-view bipolar (Fig. 4.2(h)) and unipolar (Fig. 4.2(i)) images of the leaf skeleton, we can see that the two images have identical features. This identity confirms that the multi-view Hilbert transformation followed by amplitude extraction keeps all the features of the original bipolar image. Fig. 4.2(j) compares the profiles of Figs. 4.2(h) and 4.2(i) along the dashed lines. The contrast-to-noise ratios (CNRs) of selected features, marked with numbers 1-8 in Fig. 4.2(j), are presented in Fig. 4.2(k). Clearly the full-view unipolar image has a better CNR than the bipolar image, mainly because, after the multi-view Hilbert transformation, the noise level has been lowered more than the signals.

The in-plane spatial resolutions of the multi-view PACT imaging system were also quantified by imaging 10-μm-diameter black-dyed microspheres (Polysciences Inc.) mixed in an agar gel. Fig. 4.3(a) shows a single-view unipolar PACT image of the microsphere phantom, and Fig. 4.3(b) shows an enlarged image of a single microsphere, as enclosed by a dashed box in Fig. 4.3(a). Fig. 4.3(c) shows the PA amplitude distribution along the dashed arrow y_{l1} in Fig. 4.3(b), and the Gaussian fitting result shows that the full width at half maximum (FWHM) is 89 μm, which is the lateral resolution of the single-view PACT system. With the same method, the axial resolution of the single-view PACT along the x_l direction was quantified to be 52 μm. Fig. 4.3(d) shows a full-view unipolar PACT image of the microspheres with 18 views and a 20 degree angular step size. Fig. 4.3(e) is an enlarged image of the same microsphere shown in Fig.

47

4.3(b). It is obvious that the full-view microsphere image is isotropic in the $x_l y_l$ imaging plane. Fig. 4.3(f) shows the PA amplitude distribution along the dashed arrow y_{l2} in Fig. 4.3(e), and the Gaussian fitting result shows that the FWHM value is 60 μm, less than the single-view FWHM of 89 μm along the y_{l1} direction in Fig. 4.3(b). The isotropic resolution of the full-view unipolar PACT is slightly worse than the axial resolution of the single-view PACT, due to the blurring effect of the incoherent sum in the unipolar image reconstruction process.
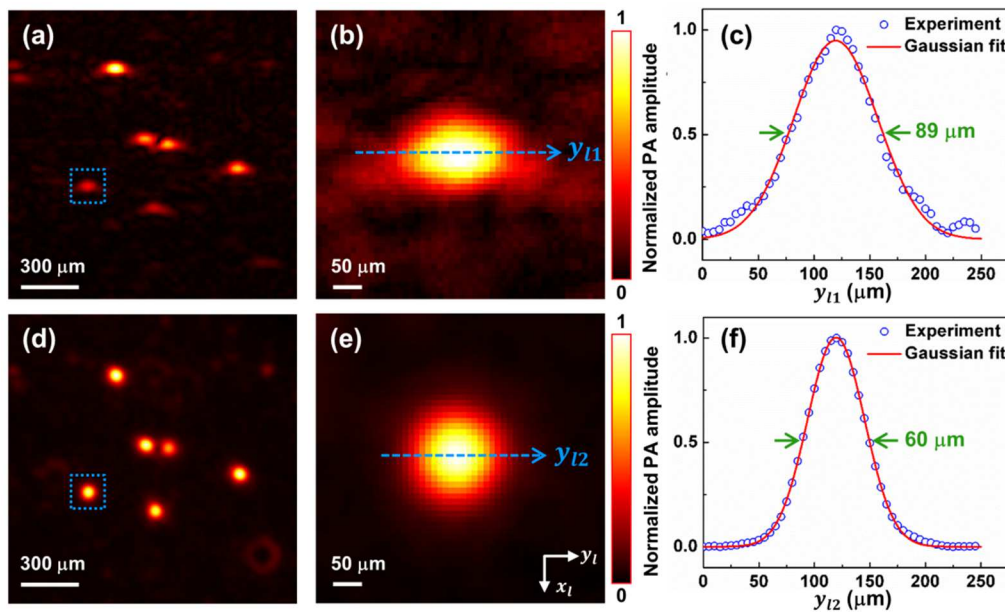
Figure 4.3 Characterization of the full-view linear-array PACT system. (a) Single-view unipolar image of 10 μm microspheres, (b) enlarged image of the single microsphere in the dashed box of (a), (c) photoacoustic amplitude distribution along the dashed line in (b), (d) full-view unipolar image of 10 μm microspheres, (e) enlarged image of a single microsphere in the dashed box of (d), and (f) photoacoustic amplitude distribution along the dashed line in (e).

With isotropic high resolution in the imaging plane, full-view linear-array PACT can resolve fine structures in biological tissues. The zebrafish is a major model organism for biomedical research, but low-frequency PACT cannot resolve its tiny features. Here we use the high-frequency full-view PACT system to perform *in vivo* imaging of a zebrafish embedded in a low gelling

temperature agarose (A9414, Sigma). All animal work was performed in compliance with Washington University's institutional animal protocols. During the scan process, the zebrafish was alive and its heart was beating. Fig. 4.4(a) shows a single-view bipolar PACT image of the zebrafish. Only the trunk vessel (TV) and part of the eye can be identified. Fig. 4.4(b) is the corresponding unipolar image of Fig. 4.4(a) obtained by Hilbert transformation and amplitude extraction along the acoustic axis. It shows a clearer boundary of the zebrafish, but still suffers from the limited-view problem. Fig. 4.4(c) is a full-view bipolar PACT image of the zebrafish with 18 views and a 20 degree angular step size. The eye now appears round, and we can begin to discern the ventral fin (VF) and dorsal fin (DF) in addition to the trunk vessel (TV). Fig. 4.4(d) is a corresponding full-view unipolar PACT image, showing clearer features, such as boundaries, tails, and tiny bones close to the trunk vessel. Although Fig. 4.4(d) looks better than Fig. 4.4(c), they actually show the same details, as proved by comparing the features of the enlarged sections from the same area. Fig. 4.4(e) shows a full-view unipolar ultrasound image of the zebrafish achieved by adding the beamformed enveloped ultrasound image at each rotation angle. Since the ultrasound image resolves mechanical contrasts, we can clearly see the swim bladders and spine. Fig. 4.4(f) is a fused image of 4.4(d) and 4.4(e), and it shows both image contrasts (mechanical and optical contrasts). We can clearly identify the trunk vessel and spine in Fig. 4.4(f).
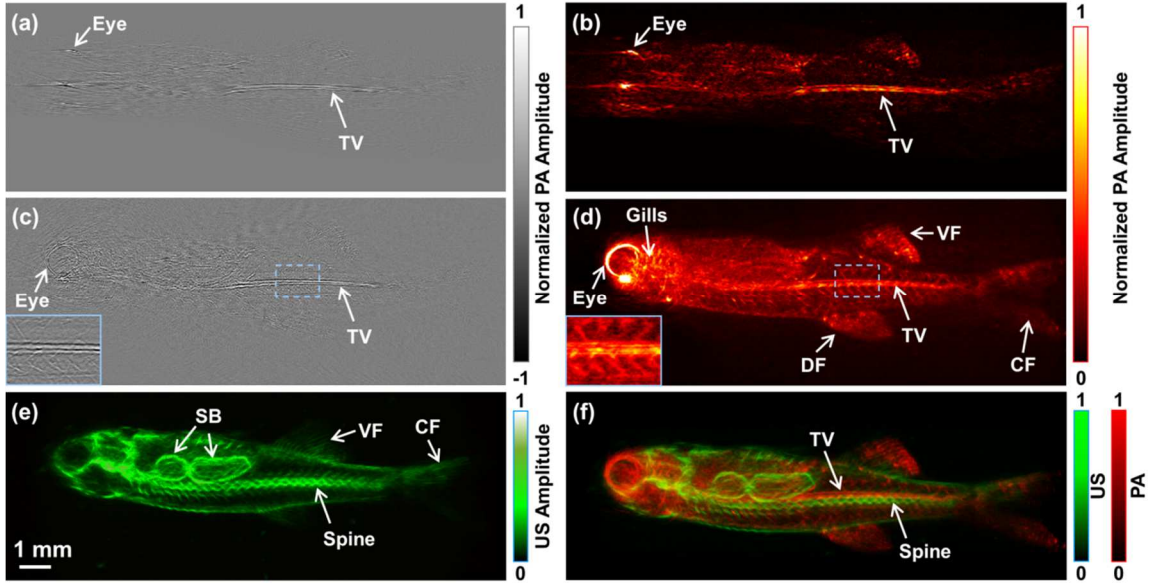
Figure 4.4 *In vivo* images of a zebrafish. (a) bipolar single-view PACT image, (b) unipolar single-view PACT image, (c) bipolar full-view PACT image with an enlarged image at the lower left corner representing the dashed area, (d) unipolar full-view PACT image with an enlarged image at the lower left corner representing the dashed area, (e) unipolar full-view ultrasound image, (f) co-registered US/PA image of the zebrafish obtained by merging (d) and (e). Note that the spine and the trunk vessel (TV) can be clearly differentiated in (f). CF, caudal fin; DF, dorsal fin; SB, swim bladders; US, ultrasound; VF, ventral fin.

Conclusions   We present a high-frequency full-view linear-array PACT imaging system paired with a novel multi-view Hilbert transformation method. The system has an isotropic spatial resolution of 60 μm within the imaging plane. Such a high resolution allows us to clearly identify different vessels and organs in a live zebrafish. Compared with the conventional FBP method, the multi-view reconstruction and Hilbert transformation method renders much clearer envelope images of the zebrafish. If the unipolar image recovered by applying the single-view Hilbert transformation along the acoustic axis and taking the absolute value represents optical absorption correctly, the multi-view Hilbert transformation images, which are achieved by linearly adding unipolar images from different views, should also represent the optical absorption correctly. The maximum imaging depth of the single-view linear-array PACT system was ~10 mm in this

study. By rotating the sample 360 degrees, we are able to image samples with diameters up to ~20 mm. Currently, the imaging speed is limited by the low repetition rate of the laser and the slow manual rotation scan. Therefore the imaging speed of full-view linear-array PACT is lower than that of circular-array PACT. However, linear-array PACT provides a low cost solution with more frequency choices. Moreover, its imaging speed can be further improved by using a faster laser system and a motorized rotation scan setup.

By applying side illumination plus elevational scanning, we will be able to acquire 3D whole-body images of small animals. Compared with whole-body PA macroscopy [73], the full-view linear-array PACT has higher in-plane image quality due to the full-view detection, but the 3D whole-body image quality is worse because of the relatively poor elevational resolution of the linear transducer array.

4.2   Inverse Linear Radon Transformation PACT

Background   Photoacoustic computed tomography (PACT) is an emerging imaging modality that ultrasonically breaks through the optical diffusion limit by combining optical contrasts and ultrasonic spatial resolution [2]. To accelerate imaging speed, PACT usually uses many ultrasonic transducer elements configured spatially to detect photoacoustic waves, and then reconstructs an image using inverse algorithms. Although curved transducer arrays, such as ring-shaped arrays[7, 8, 69], arc-shaped arrays [34], and spherical arrays [50], can obtain high-quality PACT images, they are usually customized and expensive. Moreover, they need accessibility from multiple sides of the object, limiting their applications to objects such as small animals or human breasts [7, 8, 34, 50, 69]. In comparison, one-dimensional (1D) cylindrically focused linear transducer arrays are readily available at low cost, are widely used, offer hand-held convenience, and can form images from just one side of the sample [28, 30, 31, 35, 74, 75].

However, conventional three-dimensional (3D) PACT images acquired by such a linear array through linear scans along the transducers' elevational direction have low overall image quality due to the poor elevational resolution. Here, we define the axial resolution as the spatial resolution along the acoustic axis, the lateral resolution as the spatial resolution along the row of elements of the array, and the elevational resolution as the spatial resolution along the direction normal to the B-scan image plane of the linear transducer array. The axial resolution is limited by the speed of sound of the acoustic medium and the bandwidth of the photoacoustic signals and transducer elements. The lateral resolution is mainly determined by the center frequency and the synthetic aperture of the transducer array relative to the image reconstruction region. The elevational resolution is determined by the center frequency, the element length, and the focal length of the cylindrical acoustic lens. While the lateral resolution is usually slightly worse than the axial resolution, the elevational resolution is one order of magnitude worse. Consequently, the poor elevational resolution renders conventionally stacked 3D images of low quality.

The 3D image quality can be improved with various techniques. A two-dimensional (2D) ultrasonic array might be used [76], but a 2D array costs much more than a 1D linear array. Song et al. proposed a section-illumination setup and improved the elevational resolution by 10 times over that of a single direction scan without section illumination [77]. But the section-illumination elevational resolution depends on optical focusing and degrades to the acoustically defined elevational resolution beyond one optical transport mean free path. Gateau et al. explored using a combined linear and rotation scan to achieve nearly isotropic 3D spatial resolution [38, 71, 72]. However, their configurations enclosed the object and required full perimeter access around it, which is feasible for imaging small animals but inconvenient for other applications. Recently, Schwarz et al. [78] proposed a bi-directional scan method to improve the spatial resolution, but

the resulting spatial resolution was not uniform in all directions, and taking the geometric mean of the signals from the orthogonal scans lacks physical meaning. Here we propose a new method that makes multiple elevational scans by a linear transducer array in varied probe orientations and reconstructs 3D images by using the inverse linear Radon transformation (ILRT)—a standard image reconstruction method in x-ray CT. We call this method ILRT-PACT.

Methods   The ILRT-PACT setup is shown schematically in Fig. 4.5(a). A commercial cylindrically focused linear ultrasonic transducer array with 256 elements (LZ250, 21 MHz central frequency, 11 MHz bandwidth, Visualsonics Inc., Canada) [74] serves as the photoacoustic detector. This array is integrated with an optical fiber bundle to provide dark-field optical illumination at the end of the probe. The focal length of the cylindrical acoustic lens is 15 mm. A 20 Hz laser (Brilliant, Quantel, USA) with 532 nm wavelength is coupled into the fiber bundle of the probe. The output laser pulse has an average intensity of ~ 8 mJ/cm^2 on the tissue's surface, well within the ANSI safety limit (20 mJ/cm^2). To homogenize the incident laser light and acoustically couple the photoacoustic waves, a layer of a mixture of ultrasonic gel and 1% intralipid solution is applied on the tissue's surface, which is in contact with a flexible polyethylene membrane window in the bottom of a water-filled tank. The ultrasonic transducer array is submerged in a water-filled Petri dish for acoustic coupling. A commercial photoacoustic imaging platform (Vevo LAZR, Visualsonics Inc., Canada) is used to acquire photoacoustic images. Due to the four-to-one multiplexing in the data acquisition system, the B-scan frame rate is 5 frames/s at a laser repetition rate of 20 Hz.

In ILRT-PACT, the object is rotated in increments and linearly scanned at each angular position, as shown in Fig. 4.5(a). For comparison, we call PACT with a single linear scan along the elevational direction of the transducer array at the first rotational angle "single linear-scan

PACT". In our study, ILRT-PACT used a motorized rotation stage (Produstrial LLC, USA), and each full data set contained 90 rotations with a 2° angular step size. At each rotation angle, a linear scan along the elevational direction (*x*) of the linear transducer array was performed by a motorized linear translation stage moving at 2 mm/s. With a B-scan frame rate of 5 frames/s, the step size in the elevational direction was 0.4 mm. The linear scan time at each rotation angle was 10 s, corresponding to a range of 20 mm with 50 B-scan frames. Thus each full data set contained 90×50 = 4500 B-scan frames, and the total scan time was ~16 min. [90 angles × (10 s per linear scan + 0.5 s per rotation)].
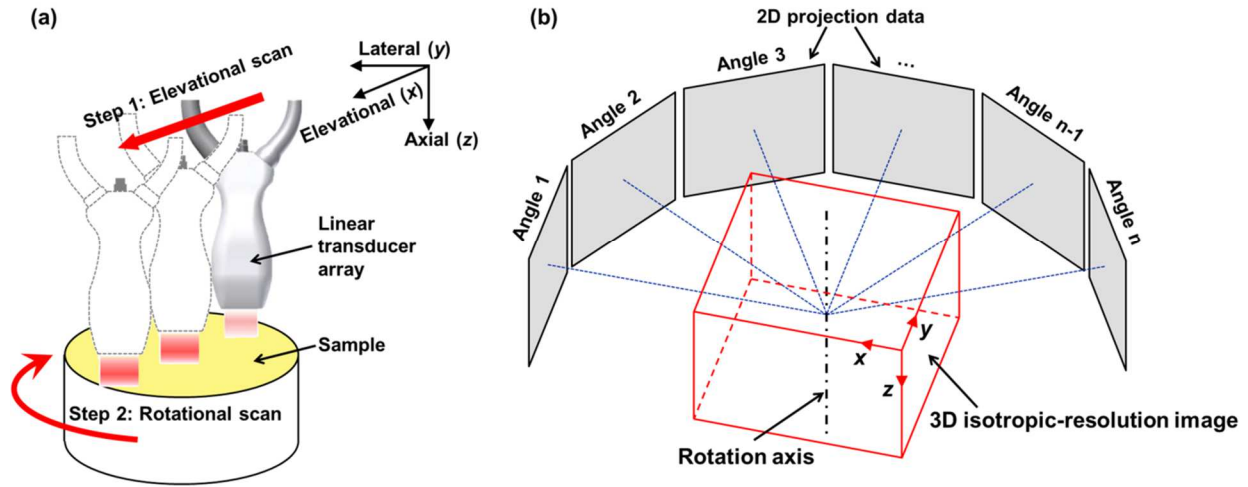
Figure 4.5 Schematic diagram of the experimental setup and the inverse linear Radon transformation process. (a) Schematic of the scanning setup of the ILRT-PACT; (b) Schematic of the inverse linear Radon transformation to reconstruct a 3D isotropic-resolution image.

To reconstruct 3D photoacoustic images from the multiple-angle data sets, we first reconstructed all the B-scan frames from the raw data received by the transducer elements, using the universal back-projection algorithm (the inverse spherical Radon transformation) [10]. Due to the band-pass frequency response of the transducer elements, the reconstructed B-scan frames present

54

bipolar (both positive and negative) pixel values. To better represent the real optical absorption, which is always non-negative, we applied the Hilbert transformation in the depth direction (z) and then took the absolute value to recover the envelope. We then integrated the B-scan frames acquired at each rotational angle through the linear Radon transformation along the elevational direction, rendering 90 2D projection images. After that, the inverse linear Radon transformation was applied to the 90 2D projections to obtain a 3D image, as shown in Fig. 4.5(b). Because the direction of the Hilbert transformation is orthogonal to those of the linear Radon transformation and inverse linear Radon transformation, the envelope extraction does not affect the linearity of either of these transformations.

Results ILRT-PACT was first demonstrated by imaging an agar gel phantom that contained three black hairs at different depths. Figs. 4.6(a) and 4.6(b) show perspective views of the 3D images acquired by single linear-scan PACT and ILRT-PACT, respectively. Figs. 4.6(c) and 4.6(d) are maximum amplitude projections (MAPs) along the depth axes (z) of the 3D images acquired by single linear-scan PACT and ILRT-PACT, respectively. Due to the sparse angular sampling, faint ray-like artifacts appear in Fig. 4.6(d) as indicated by arrows; however, they can be alleviated by increasing angular sampling at the expense of data acquisition time. Figs. 4.6(e) and 4.6(f) show corresponding 2D projection images from single linear-scan PACT and ILRT-PACT, respectively. There is not much difference between the 2D projection images on the yz plane. However, on the xy plane, not only are the line features of the ILRT-PACT image sharper than those of the single linear-scan PACT image, but also the spatial resolution along the elevational direction (x) is greatly improved. The spatial resolution along any other direction on the xy plane is also improved accordingly. As will be quantified later, in single

55

linear-scan PACT the spatial resolutions in the *xy* plane are anisotropic, but those in ILRT-PACT

are isotropic, hence the improved images.
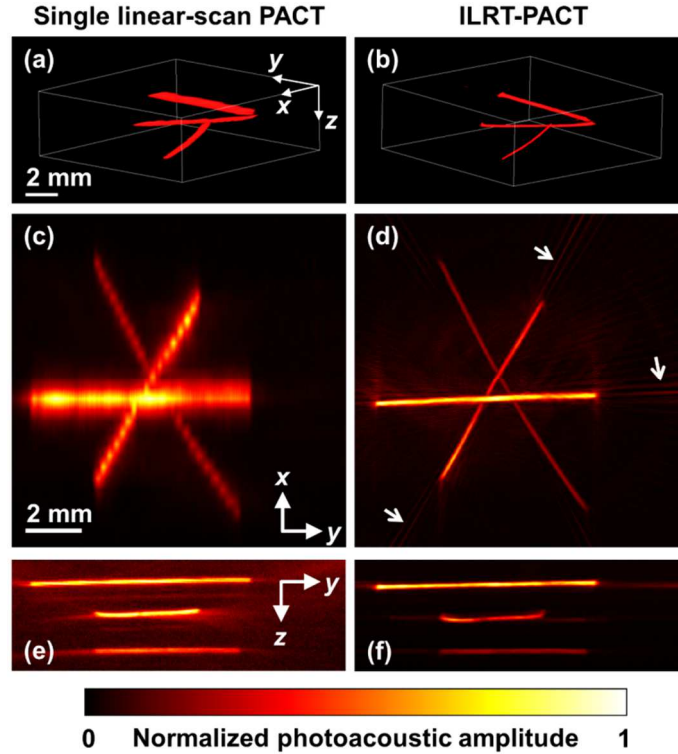
Figure 4.6 Comparison of single linear-scan PACT and the ILRT-PACT images of a hair phantom. Snapshots from the 3D animations of the single linear-scan PACT image (a) and ILRT-PACT image (b). Maximum amplitude projections (MAPs) along the depths of the single linear-scan PACT image (c) and ILRT-PACT image (d). 2D projection data of single linear-scan PACT image (e) and ILRT-PACT image (f).

To quantitatively study the elevational resolution improvement, we imaged an agar gel phantom

containing 10 μm diameter microspheres. Figs. 4.7(a) and 4.7(b) are snapshots of 3D images

acquired using single linear-scan PACT and ILRT-PACT, respectively. Figs. 4.7(c) and 4.7(d)

compare the MAPs of the 3D images. While microspheres are stretched in the elevational

direction (*x*) in the single linear-scan PACT image, they are isotropic in the ILRT-PACT image,

as further proved by Fig. 4.7(e), which is the enlarged MAP image of the microsphere marked by

a square box in Fig. 4.7(d).

56
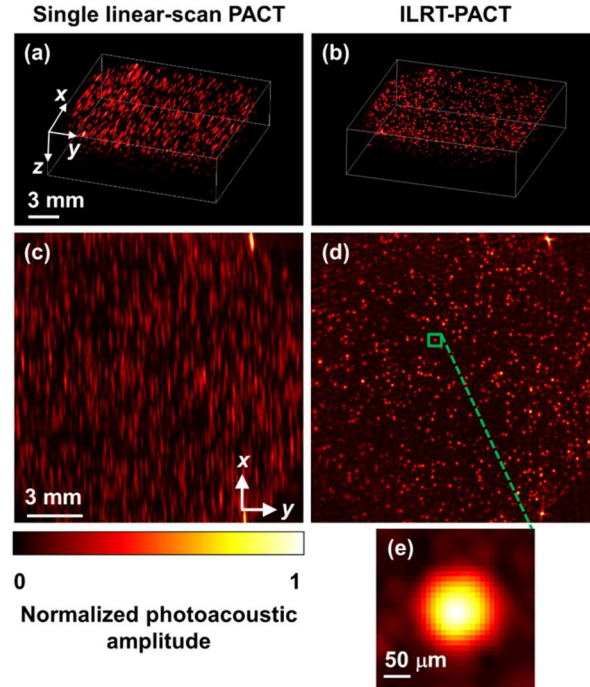
Figure 4.7 Comparison of single linear-scan PACT and the ILRT-PACT images of an agar gel phantom containing microspheres. Snapshots from 3D animations of the single linear-scan PACT image (a) and ILRT-PACT image (b). Maximum amplitude projections (MAPs) along the depth axes of the single linear-scan PACT image (c) and ILRT-PACT image (d).

Because the microspheres have a diameter much smaller than the spatial resolution of the PACT systems, they can be treated as point targets for the quantification of the system's resolution. Fig. 4.8 shows the relationship between the elevational resolution and imaging depth for both single linear-scan PACT and ILRT-PACT. As expected, the conventional elevational resolution changes with the imaging depth because the resolution is determined by the cylindrical acoustic lens. The finest single linear-scan elevational resolution in the cylindrical acoustic focal zone is ~500 μm, at an imaging depth of 15.0 mm. After the inverse linear Radon transformation, the elevational resolution is no longer determined by the acoustic lens but limited by the original lateral resolution along the y direction; as a result, it remains at a stable value, around 130 μm. Fig. 4.8 also shows that the elevational resolution improvement changes with the distance from

the cylindrical acoustic focal point, from 9.4 times to 3.8 times at corresponding depths of 8.3

mm (farthest from the focus) and 15.0 mm (at the focus).
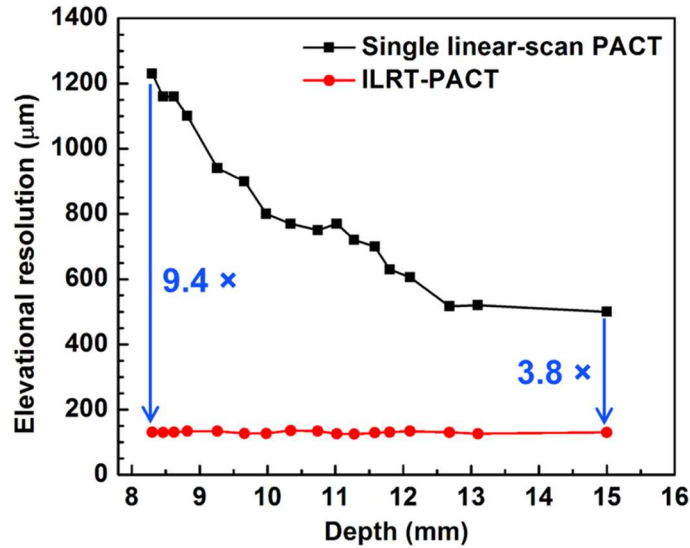
Figure 4.8 Elevational resolution of single linear-scan PACT and ILRT-PACT at different imaging depths, where the cylindrical acoustic focal point is at 15.0 mm.

The superior resolution isotropy can greatly improve the 3D image quality. With convenient

single-side access to the object, ILRT-PACT can image the mouse brain *in vivo* from the top.

Here we imaged the brain of a 30-day-old mouse (Hsd: ND4, Harlan Laboratories Inc., USA) *in*

vivo with the scalp intact but the hair removed. Figs. 4.9(a) and 4.9(b) show the 3D images

acquired by single linear-scan PACT and ILRT-PACT, respectively; Figs. 4.9(c) and 4.9(d) are

corresponding MAPs of the 3D images. Obviously the ILRT-PACT images, with their improved

spatial resolution, show features much more clearly. Fig. 4.9(e) is a photograph of the mouse

brain taken after the experiment with the scalp removed. The MAP image from ILRT-PACT

clearly shows the cortical vasculature, such as the superior sagittal sinus (SSS) and the transverse

sinus (TS). Fig. 4.9(f), a cross-sectional image of the ILRT-PACT image along the dashed line in Fig. 4.9(d), reveals the two-layer structure of the uppermost portion of the mouse brain.
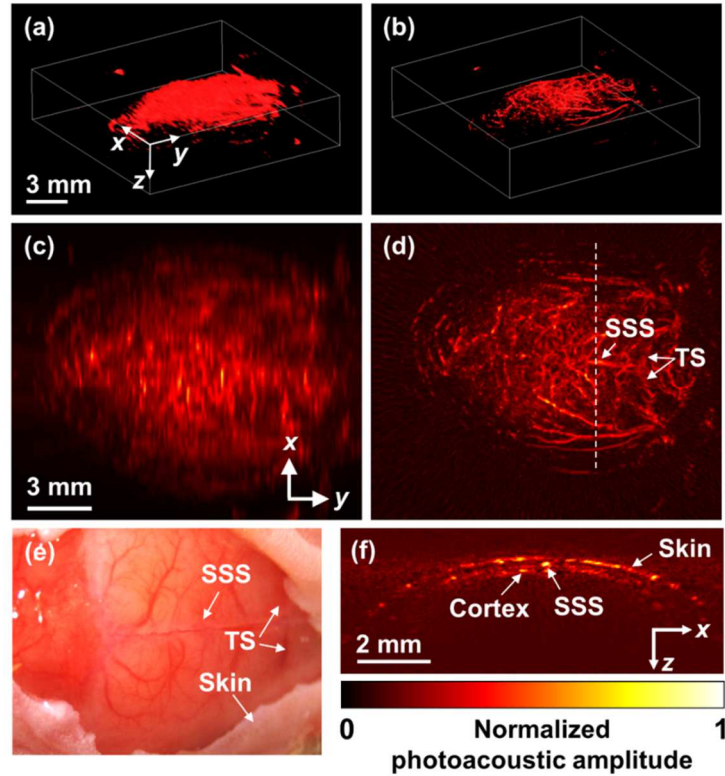
Figure 4.9 *In vivo* mouse brain images acquired by single linear-scan PACT and ILRT-PACT. Snapshots from 3D animations of the single linear-scan PACT image (a) and ILRT-PACT image (b). Maximum amplitude projections (MAPs) along the depths of the single linear-scan PACT image (c) and ILRT-PACT image (d). (e) Photograph of the mouse brain taken after the experiment, with the scalp removed. (f) Cross-sectional image of the mouse brain along the dashed line in (d). SSS, superior sagittal sinus; TS, transverse sinus.

Discussions   Currently the imaging speed of ILRT-PACT is still low (~16 min) due to the dense rotational scan, but this time can be improved by using a laser with a higher repetition rate. The limited-view problem [47] still exists because ILRT-PACT has a limited detection aperture when acquiring images from a single side of the object. However, the one-sided accessibility enables convenient ILRT-PACT imaging of large anatomical sites such as large animals and human brains.

4.3 Conclusions

We present a multi-view high-frequency PACT imaging system implemented with a commercial 40-MHz central frequency linear transducer array. By rotating the object through multiple angles with respect to the linear transducer array, we acquired full-view photoacoustic pressure measurements. Further, to quantify the unipolar initial pressures and overcome the limitations of the single-view Hilbert transformation, we developed a multi-view Hilbert transformation method. The in-plane spatial resolution of this full-view linear-array PACT was quantified to be isotropically 60 μm within a 10×10 mm^2 field of view. The system was demonstrated by imaging both a leaf skeleton and a zebrafish *in vivo*.

We also developed an ILRT-PACT method and system that provide isotropic resolution for greatly improved 3D imaging quality. The maximum experimentally verified elevational resolution improvement over single linear-scan PACT is 9.4 times at an imaging depth of 8.3 mm, and the improvement increases with the distance from the elevational focal point. *In vivo* mouse brain images have been successfully acquired using the ILRT-PACT system. This technology can be applied to all linear-array PACT imaging systems that have poor elevational resolution.

Chapter 5: Summary and Outlook

5.1 Summary

This dissertation has described advances in high-frequency linear-array OR-PAM and linear-array PACT. We realized technical advancements to MFOR-PAM, explored broadening the detection view angles of linear-array PACT, and developed two multi-view linear-array PACTs with higher image quality and spatial resolutions.

In Chapter 2, we first achieved a 1D-MFOR-PAM working in reflection mode. Compared with transmission-mode MFOR-PAM, which can image only thin samples, reflection-mode 1D-MFOR-PAM is universally applicable to all biomedical samples. With a 30 MHz linear ultrasonic transducer array, we achieved 16 μm lateral resolution and 25 μm axial resolution, as well as 0.7 mm maximum imaging depth in normal tissue. The combination of multiple optical foci and the ultrasonic transducer array reduced the lateral scanning range to only one pitch of the microlens array. The imaging time to acquire a data set of 600×500×200 voxels was ~2.5 min, about 20 times faster than single-focus OR-PAM with mechanical scanning. As an example application, we demonstrated the reflection-mode MFOR-PAM by imaging a mouse ear and mouse brain *in vivo*. We also presented a two dimensional multifocal photoacoustic microscopy (2D-MFOR-PAM), which utilizes a 2D microlens array with 40 × 40 microlenses, and a 30 MHz commercial linear ultrasonic transducer array. The 2D-MFOR-PAM allows us to acquire an image with a field of view of 10 mm × 10 mm in a constant time, in our case, 51 sec, while scanning only a small range of 250 μm × 250 μm. The field of view can be potentially enlarged by using a 2D microlens array with imaging speed unchanged.

In Chapter 3, we demonstrated two innovative methods to broaden the detection view angle of linear-array PACT. In the first method, two planar acoustic reflectors triple the detection view angle from 80 degrees to 240 degrees, while maintaining the original imaging speed. A dehydrated leaf skeleton with complex features was successfully imaged to demonstrate the feasibility of the two acoustic reflectors. The second method is a universally applicable ultrasonic thermal encoding method which was proposed to achieve full-view linear-array PACT images. A mouse ear image was acquired *in vivo* to validate the ultrasonic thermal encoding concept, showing dramatically enhanced imaging of arbitrarily oriented blood vessels.

In Chapter 4, we developed two multi-view linear-array PACTs, aiming to reveal the accurate optical absorption and improve the spatial resolutions. A multi-view Hilbert transformation algorithm was developed and applied to the full-view linear-array PACT data, rendering much clearer envelope images than the original bipolar images. The in-plane spatial resolution is 60 μm and isotropic. A linear-rotational scan was innovatively applied on the linear-array PACT, dramatically improving the elevational resolution by almost ten times. The so-called inverse linear Radon transformation achieved isotropic spatial resolutions at each depth plane. Due to the improved spatial resolutions, *in vivo* intact mouse brain images showed much higher image quality than images from conventional PACT.

5.2 Outlook

The reflection-mode MFOR-PAM offers a high imaging speed, which can be further improved by eliminating the 6:1 multiplexer and using a higher PRR laser. Optical scanning within one pitch in the lateral direction can further improve the imaging speed by several times. A more densely packed microlens array with a smaller pitch might improve the imaging speed, but this usually means a shorter working distance if we want to maintain the NA or lateral resolution.

Other multifocal designs might be developed to provide both a high NA and long working distance.

We increased the detection view angle of linear-array PACT by using two planar acoustic reflectors. Currently the double-reflector PACT has not achieved 360-degree (i.e., full-view) detection due to the limited receiving angle of the single transducer element, but it will be possible to achieve a full view in the future by using linear transducer arrays with larger element receiving angles and wider apertures. Ultrasonic thermal encoding technology allows linear-array PACT to acquire full-view images at the expense of longer acquisition time. In the future, faster PA imaging systems and shorter heating times can be used to improve the imaging speed. The thermal encoding in this work can potentially be implemented on a high-intensity focused ultrasound (HIFU) treatment system to provide PA imaging capability during treatment. Since some HIFU setups have dynamic focusing capability in both the depth and lateral directions, it becomes possible to achieve an electronic thermal encoding scan, instead of a mechanical scan.

The multi-view Hilbert transformation improves the image quality of linear-array PACT, but the imaging speed of full-view linear-array PACT is lower than that of circular-array PACT due to the manual circular scan. This speed can be increased by using a faster laser system and a motorized rotation scan setup. The linear-rotational scan with the inverse linear Radon transformation help the linear-array PACT achieve improved isotropic resolutions at each depth plane. Therefore this technology can be applied to all linear-array PACT imaging systems that have poor elevational resolution. However, the imaging speed of ILRT-PACT is still low (~16 min) due to the dense rotational scan, but this time can be improved by using a laser with a higher repetition rate.

References

1. B. Alexander Graham, "ART. XXXIV.--On the Production and Reproduction of Sound by Light," American Journal of Science (1880-1910) **20**, 305 (1880).
2. L. V. Wang and S. Hu, "Photoacoustic Tomography: In Vivo Imaging from Organelles to Organs," Science **335**, 1458-1462 (2012).
3. K. Maslov, H. F. Zhang, S. Hu, and L. V. Wang, "Optical-resolution photoacoustic microscopy for in vivo imaging of single capillaries," Opt. Lett. **33**, 929-931 (2008).
4. S. Hu, K. Maslov, and L. V. Wang, "Second-generation optical-resolution photoacoustic microscopy with improved sensitivity and speed," Opt. Lett. **36**, 1134-1136 (2011).
5. C. P. Favazza, O. Jassim, L. A. Cornelius, and L. V. Wang, "In vivo photoacoustic microscopy of human cutaneous microvasculature and a nevus," J. Biomed. Opt. **16**, 016015-016015 (2011).
6. K. Maslov, G. Stoica, and L. V. Wang, "In vivo dark-field reflection-mode photoacoustic microscopy," Opt. Lett. **30**, 625-627 (2005).
7. J. Xia, Z. Guo, K. Maslov, A. Aguirre, Q. Zhu, C. Percival, and L. V. Wang, "Three-dimensional photoacoustic tomography based on the focal-line concept," J. Biomed. Opt. **16**, 090505 (2011).
8. J. Xia, M. R. Chatni, K. Maslov, Z. Guo, K. Wang, M. Anastasio, and L. V. Wang, "Whole-body ring-shaped confocal photoacoustic computed tomography of small animals in vivo," J. Biomed. Opt. **17**, 050506 (2012).
9. J.-M. Yang, C. Favazza, R. Chen, J. Yao, X. Cai, K. Maslov, Q. Zhou, K. K. Shung, and L. V. Wang, "Simultaneous functional photoacoustic and ultrasonic endoscopy of internal organs in vivo," Nat Med **18**, 1297-1302 (2012).
10. M. Xu and L. V. Wang, "Universal back-projection algorithm for photoacoustic computed tomography," Physical Review E **71**, 016706 (2005).
11. G. Li, K. I. Maslov, and L. V. Wang, "Reflection-mode multifocal optical-resolution photoacoustic microscopy," J. Biomed. Opt. **18**, 030501-030501 (2013).
12. L. V. Wang, "Multiscale photoacoustic microscopy and computed tomography," Nature photonics **3**, 503-509 (2009).
13. J. Yao, K. I. Maslov, E. R. Puckett, K. J. Rowland, B. W. Warner, and L. V. Wang, "Double-illumination photoacoustic microscopy," Opt. Lett. **37**, 659-661 (2012).
14. P. Hajireza, W. Shi, and R. J. Zemp, "Label-free in vivo fiber-based optical-resolution photoacoustic microscopy," Opt. Lett. **36**, 4107-4109 (2011).
15. A. Krumholz, L. Wang, J. Yao, and L. V. Wang, "Functional photoacoustic microscopy of diabetic vasculature," J. Biomed. Opt. **17**, 060502-060501 (2012).
16. J. Yao, C.-H. Huang, L. Wang, J.-M. Yang, L. Gao, K. I. Maslov, J. Zou, and L. V. Wang, "Wide-field fast-scanning photoacoustic microscopy based on a water-immersible MEMS scanning mirror," J. Biomed. Opt. **17**, 080505-080501 (2012).
17. C. Zhang, K. Maslov, and L. V. Wang, "Subwavelength-resolution label-free photoacoustic microscopy of optical absorption in vivo," Opt. Lett. **35**, 3195-3197 (2010).
18. C. Zhang, K. Maslov, S. Hu, R. Chen, Q. Zhou, K. K. Shung, and L. V. Wang, "Reflection-mode submicron-resolution in vivo photoacoustic microscopy," J. Biomed. Opt. **17**, 020501-020504 (2012).

19.   P. Hajireza, W. Shi, and R. J. Zemp, "Real-time handheld optical-resolution photoacoustic microscopy," Opt. Express **19**, 20097-20102 (2011).
20.   L. Song, K. Maslov, and L. V. Wang, "Multifocal optical-resolution photoacoustic microscopy in vivo," Opt. Lett. **36**, 1236-1238 (2011).
21.   R. J. Zemp, L. Song, R. Bitton, K. K. Shung, and L. V. Wang, "Realtime photoacoustic microscopy in vivo with a 30-MHz ultrasound array transducer," Opt. Express **16**, 7915-7928 (2008).
22.   S. Hu, K. Maslov, V. Tsytsarev, and L. V. Wang, "Functional transcranial brain imaging by optical-resolution photoacoustic microscopy," J. Biomed. Opt. **14**(2009).
23.   Z. Xie, S. Jiao, H. F. Zhang, and C. A. Puliafito, "Laser-scanning optical-resolution photoacoustic microscopy," Opt. Lett. **34**, 1771-1773 (2009).
24.   S. Hu, B. Rao, K. Maslov, and L. V. Wang, "Label-free photoacoustic ophthalmic angiography," Opt. Lett. **35**, 1-3 (2010).
25.   G. Ku, K. Maslov, L. Li, and L. V. Wang, "Photoacoustic microscopy with 2-μm transverse resolution," J. Biomed. Opt. **15**, 021302-021302 (2010).
26.   H. Wang, X. Yang, Y. Liu, B. Jiang, and Q. Luo, "Reflection-mode optical-resolution photoacoustic microscopy based on a reflective objective," Optics Express **21**, 24210-24218 (2013).
27.   J. Xia, G. Li, L. Wang, M. Nasiriavanaki, K. Maslov, J. A. Engelbach, J. R. Garbow, and L. V. Wang, "Wide-field two-dimensional multifocal optical-resolution photoacoustic-computed microscopy," Optics Letters **38**, 5236-5239 (2013).
28.   G. Li, J. Xia, K. Wang, K. Maslov, M. A. Anastasio, and L. V. Wang, "Tripling the detection view of high-frequency linear-array-based photoacoustic computed tomography by using two planar acoustic reflectors," Quantitative Imaging in Medicine and Surgery **5**, 57-62 (2015).
29.   L. Wang, G. Li, J. Xia, and L. V. Wang, "Ultrasonic-heating-encoded photoacoustic tomography with virtually augmented detection view," Optica **2**, 307-312 (2015).
30.   L. Song, K. Maslov, K. K. Shung, and L. V. Wang, "Ultrasound-array-based real-time photoacoustic microscopy of human pulsatile dynamics in vivo," J. Biomed. Opt. **15**, 021303 (2010).
31.   C. Kim, T. N. Erpelding, K. Maslov, L. Jankovic, W. J. Akers, L. Song, S. Achilefu, J. A. Margenthaler, M. D. Pashley, and L. V. Wang, "Handheld array-based photoacoustic probe for guiding needle biopsy of sentinel lymph nodes," J. Biomed. Opt. **15**, 046010 (2010).
32.   C. Kim, T. N. Erpelding, L. Jankovic, and L. V. Wang, "Performance benchmarks of an array-based hand-held photoacoustic probe adapted from a clinical ultrasound system for non-invasive sentinel lymph node imaging," Philosophical Transactions of the Royal Society A: Mathematical, Physical and Engineering Sciences **369**, 4644-4650 (2011).
33.   J. Gamelin, A. Maurudis, A. Aguirre, F. Huang, P. Guo, L. V. Wang, and Q. Zhu, "A real-time photoacoustic tomography system for small animals," Opt. Express **17**, 10489-10498 (2009).
34.   H.-P. Brecht, R. Su, M. Fronheiser, S. A. Ermilov, A. Conjusteau, and A. A. Oraevsky, "Whole-body three-dimensional optoacoustic tomography system for small animals," J. Biomed. Opt. **14**, 064007 (2009).

35.   J. Yuan, G. Xu, Y. Yu, Y. Zhou, P. L. Carson, X. Wang, and X. Liu, "Real-time photoacoustic and ultrasound dual-modality imaging system facilitated with graphics processing unit and code parallel optimization," J. Biomed. Opt. **18**, 086001 (2013).

36.   D. W. Yang, D. Xing, S. H. Yang, and L. Z. Xiang, "Fast full-view photoacoustic imaging by combined scanning with a linear transducer array," Optics Express **15**, 15566-15575 (2007).

37.   R. A. Kruger, J. W. L. Kiser, D. R. Reinecke, and G. A. Kruger, "Thermoacoustic computed tomography using a conventional linear transducer array," Medical Physics **30**, 856-860 (2003).

38.   J. Gateau, M. A. A. Caballero, A. Dima, and V. Ntziachristos, "Three-dimensional optoacoustic tomography using a conventional ultrasound linear detector array: Whole-body tomographic system for small animals," Medical Physics **40**, 013302-013311 (2013).

39.   J. Gateau, T. Chaigne, O. Katz, S. Gigan, and E. Bossy, "Improving visibility in photoacoustic imaging using dynamic speckle illumination," Optics Letters **38**, 5188-5191 (2013).

40.   S. Ma, S. Yang, and H. Guo, "Limited-view photoacoustic imaging based on linear-array detection and filtered mean-backprojection-iterative reconstruction," Journal of Applied Physics **106**, 123104 (2009).

41.   L. V. Wang and X. Yang, "Boundary conditions in photoacoustic tomography and image reconstruction," J. Biomed. Opt. **12**, 014027 (2007).

42.   B. T. Cox, S. R. Arridge, and P. C. Beard, "Photoacoustic tomography with a limited-aperture planar sensor and a reverberant cavity," Inverse Problems **23**, S95 (2007).

43.   B. Huang, J. Xia, K. Maslov, and L. V. Wang, "Improving limited-view photoacoustic tomography with an acoustic reflector," J. Biomed. Opt. **18**, 110505 (2013).

44.   H. Chao, W. Kun, N. Liming, L. V. Wang, and M. A. Anastasio, "Full-Wave Iterative Image Reconstruction in Photoacoustic Tomography With Acoustically Inhomogeneous Media," IEEE Transactions on Medical Imaging **32**, 1097-1110 (2013).

45.   Z. Jin, M. A. Anastasio, P. J. La Riviere, and L. V. Wang, "Effects of Different Imaging Models on Least-Squares Image Reconstruction Accuracy in Photoacoustic Tomography," IEEE Transactions on Medical Imaging **28**, 1781-1790 (2009).

46.   J. Xia, C. Huang, K. Maslov, M. A. Anastasio, and L. V. Wang, "Enhancement of photoacoustic tomography by ultrasonic computed tomography based on optical excitation of elements of a full-ring transducer array," Optics Letters **38**, 3140-3143 (2013).

47.   Y. Xu, L. V. Wang, G. Ambartsoumian, and P. Kuchment, "Reconstructions in limited-view thermoacoustic tomography," Medical Physics **31**, 724-733 (2004).

48.   Z. Guo, L. Li, and L. V. Wang, "On the speckle-free nature of photoacoustic tomography," Medical Physics **36**, 4084-4088 (2009).

49.   C. Li, A. Aguirre, J. Gamelin, A. Maurudis, Q. Zhu, and L. V. Wang, "Real-time photoacoustic tomography of cortical hemodynamics in small animals," J. Biomed. Opt. **15**, 010509-010509 (2010).

50.   R. A. Kruger, C. M. Kuzmiak, R. B. Lam, D. R. Reinecke, S. P. Del Rio, and D. Steed, "Dedicated 3D photoacoustic breast imaging," Medical Physics **40**, 113301 (2013).

51.   L. Wang, K. Maslov, W. Xing, A. Garcia-Uribe, and L. V. Wang, "Video-rate functional photoacoustic microscopy at depths," J. Biomed. Opt. **17**, 106007-106001 (2012).

52.   L. Nie, X. Cai, K. Maslov, A. Garcia-Uribe, M. A. Anastasio, and L. V. Wang, "Photoacoustic tomography through a whole adult human skull with a photon recycler," J. Biomed. Opt. **17**, 110506-110506 (2012).

53.   D. J. Grootendorst, J. Jose, M. W. Wouters, H. van Boven, J. Van der Hage, T. G. Van Leeuwen, W. Steenbergen, S. Manohar, and T. J. M. Ruers, "First experiences of photoacoustic imaging for detection of melanoma metastases in resected human lymph nodes," Lasers in Surgery and Medicine **44**, 541-549 (2012).

54.   L. Wang, K. Maslov, and L. V. Wang, "Single-cell label-free photoacoustic flowoxigraphy in vivo," Proceedings of the National Academy of Sciences **110**, 5759-5764 (2013).

55.   X. Liu, D. Peng, X. Ma, W. Guo, Z. Liu, D. Han, X. Yang, and J. Tian, "Limited-view photoacoustic imaging based on an iterative adaptive weighted filtered backprojection approach," Applied Optics **52**, 3477-3483 (2013).

56.   P. M. Meaney, T. Zhou, M. W. Fanning, S. D. Geimer, and K. D. Paulsen, "Microwave thermal imaging of scanned focused ultrasound heating: Phantom results," International Journal of Hyperthermia **24**, 523-536 (2008).

57.   M. Pramanik and L. V. Wang, "Thermoacoustic and photoacoustic sensing of temperature," J. Biomed. Opt. **14**(2009).

58.   L. Gao, L. Wang, C. Li, Y. Liu, H. Ke, C. Zhang, and L. V. Wang, "Single-cell photoacoustic thermometry," J. Biomed. Opt. **18**, 026003-026003 (2013).

59.   L. Wang, J. Yao, K. I. Maslov, W. Xing, and L. V. Wang, "Ultrasound-heated photoacoustic flowmetry," J. Biomed. Opt. **18**, 117003-117003 (2013).

60.   L. Wang, J. Xia, J. Yao, K. I. Maslov, and L. V. Wang, "Ultrasonically Encoded Photoacoustic Flowgraphy in Biological Tissue," Physical Review Letters **111**, 204301 (2013).

61.   L. Wang, C. Zhang, and L. V. Wang, "Grueneisen Relaxation Photoacoustic Microscopy," Physical Review Letters **113**, 174301 (2014).

62.   L. V. Wang, "Tutorial on photoacoustic microscopy and computed tomography," Selected Topics in Quantum Electronics, IEEE Journal of **14**, 171-179 (2008).

63.   G. J. Diebold, T. Sun, and M. I. Khan, "Photoacoustic monopole radiation in one, two, and three dimensions," Physical Review Letters **67**, 3384 (1991).

64.   B. E. Treeby and B. T. Cox, "k-Wave: MATLAB toolbox for the simulation and reconstruction of photoacoustic wave fields," J. Biomed. Opt. **15**, 021314-021314-021312 (2010).

65.   B. E. Treeby, J. Jaros, A. P. Rendell, and B. T. Cox, "Modeling nonlinear ultrasound propagation in heterogeneous media with power law absorption using a k-space pseudospectral method," The Journal of the Acoustical Society of America **131**, 4324-4336 (2012).

66.   L. V. Wang and H.-i. Wu, *Biomedical optics: principles and imaging* (Wiley. com, 2012).

67.   A. Prost, A. Funke, M. Tanter, J.-F. Aubry, and E. Bossy, "Photoacoustic-guided ultrasound therapy with a dual-mode ultrasound array," J. Biomed. Opt. **17**, 0612051-0612056 (2012).

68.   G. Li, L. Li, L. Zhu, J. Xia, and L. V. Wang, "Multiview Hilbert transformation for full-view photoacoustic computed tomography using a linear array," J. Biomed. Opt. **20**, 066010-066010 (2015).

69.   M. Nasiriavanaki, J. Xia, H. Wan, A. Q. Bauer, J. P. Culver, and L. V. Wang, "High-resolution photoacoustic tomography of resting-state functional connectivity in the mouse brain," Proceedings of the National Academy of Sciences **111**, 21-26 (2013).

70.   A. Dima, N. C. Burton, and V. Ntziachristos, "Multispectral optoacoustic tomography at 64, 128, and 256 channels," J. Biomed. Opt. **19**, 036021 (2014).

71.   J. Gateau, A. Chekkoury, and V. Ntziachristos, "High-resolution optoacoustic mesoscopy with a 24 MHz multidetector translate-rotate scanner," J. Biomed. Opt. **18**, 106005 (2013).

72.   J. Gateau, A. Chekkoury, and V. Ntziachristos, "Ultra-wideband three-dimensional optoacoustic tomography," Optics Letters **38**, 4671-4674 (2013).

73.   M. Jeon, J. Kim, and C. Kim, "Multiplane spectroscopic whole-body photoacoustic imaging of small animals in vivo," Med Biol Eng Comput, 1-12 (2014).

74.   A. Needles, A. Heinmiller, J. Sun, C. Theodoropoulos, D. Bates, D. Hirson, M. Yin, and F. S. Foster, "Development and initial application of a fully integrated photoacoustic micro-ultrasound system," IEEE Transactions on Ultrasonics, Ferroelectrics and Frequency Control **60**, 888-897 (2013).

75.   T.-C. Hsiao, Y.-Y. Cheng, W.-T. Tein, S.-B. Luo, D.-Y. Chiou, R.-J. Chung, and M.-L. Li, "Deep-penetration photoacoustic array imaging of calcifications," J. Biomed. Opt. **18**, 066002-066002 (2013).

76.   Y. Wang, T. N. Erpelding, L. Jankovic, Z. Guo, J.-L. Robert, G. David, and L. V. Wang, "In vivo three-dimensional photoacoustic imaging based on a clinical matrix array ultrasound probe," J. Biomed. Opt. **17**, 061208 (2012).

77.   L. Song, K. Maslov, and L. V. Wang, "Section-illumination photoacoustic microscopy for dynamic 3D imaging of microcirculation in vivo," Opt. Lett. **35**, 1482-1484 (2010).

78.   M. Schwarz, A. Buehler, and V. Ntziachristos, "Isotropic high resolution optoacoustic imaging with linear detector arrays in bi-directional scanning," Journal of Biophotonics **8**, 60-70 (2014).

Vita

Guo Li

Degrees   Ph.D., Mechanical Engineering
Washington University in St. Louis
August 2015

M.S., Engineering Physics
Tsinghua University
June 2009

B.S., Mechanical Engineering
Tsinghua University
June 2006

Publications   **Guo Li**, Jun Xia, Lei Li, Lidai Wang and Lihong V. Wang, "Linear-rotational scanning of a focused linear ultrasound array to achieve isotropic resolution of photoacoustic computed tomography", *Journal of Biomedical Optics*. (under review)

Guo Li, Lei Li, Liren Zhu, Jun Xia and Lihong V. Wang, "Multi-view Hilbert transformation for full-view photoacoustic computed tomography using a linear array", *Journal of Biomedical Optics*. (accepted)

[Lidai Wang, **Guo Li**], Jun Xia and Lihong V. Wang, "Ultrasonic heating encoded photoacoustic tomography with virtually augmented detection view", *Optica*, 2(4), 307-312 (2015).

      ([] denotes equal contribution.)

[Yong Zhou, **Guo Li**], Liren Zhu, Chiye Li, Lynn A. Cornelius and Lihong V. Wang, "Handheld photoacoustic probe to detect both melanoma depth and volume at high speed in vivo", *Journal of Biophotonics*. (accepted, in press)

Guo Li, Jun Xia, Konstantin I. Maslov and Lihong V. Wang, "Tripling the detection view of high-frequency linear-array-based photoacoustic computed tomography by using two planar acoustic reflectors", *Quantitative Imaging in Medicine and Surgery*, 5(1), 57-62 (2015).

Jun Xia, **Guo Li**, Lidai Wang, Mohammadreza Nasiriavanaki, Konstantin Maslov, John A. Engelbach, Joel R. Garbow and Lihong V. Wang, "Wide-field two-dimensional multifocal optical-resolution photoacoustic-computed microscopy", *Optics Letters*, 38(24), 5236(2013)

Guo Li, Konstantin I. Maslov and Lihong V. Wang, "Reflection-mode multifocal optical-resolution photoacoustic microscopy", *Journal of Biomedical Optics* 18(3), 030501 (2013)

He-Ping Li, Liyan Wang, **Guo Li**, Lihua Jin, Peisi Le, Hongxin Zhao, Xin-Hui Xing, Cheng-Yu Bao, "Manipulation of Lipase Activity by the Helium Radio-Frequency, Atmospheric-Pressure Glow Discharge Plasma Jet", *Plasma Processes and Polymers* 8(3), 224-229 (2011)

Guo Li, Pei-Si Le, He-Ping Li and Cheng-Yu Bao, "Effects of the shielding cylinder and substrate on the characteristics of an argon radio-frequency atmospheric glow discharge plasma jet", *Journal of Applied Physics* 107, 103304 (2010)

Peisi Le, **Guo Li**, Sen Wang, Heping Li and Chengyu Bao, "Characteristics of kilohertz-ignited, radio-frequency atmospheric-pressure dielectric barrier discharges in argon", *Applied Physics Letters* 95, 201501 (2009)

Guo Li, He-Ping Li, Liyan Wang, Sen Wang, Hongxin Zhao, Wen-Ting Sun, Xin-Hui Xing and Cheng-Yu Bao, "Genetic Effects of Radio-frequency, Atmospheric-pressure Glow Discharges with Helium", *Applied Physics Letters* 92, 221504 (2008)

Guo Li, Heping Li, Wenting Sun, Sen Wang, Zhe Tian and Chengyu Bao, "Discharge features of radio-frequency, atmospheric-pressure cold plasmas under an intensified local electric field", *Journal of Physics D: Applied Physics* 41, 202001 (2008)

He-Ping Li, **Guo Li**, Sen Wang, Pei-Si Le and Cheng-Yu Bao, "Radio-frequency glow discharges of different gases using bare metallic electrodes at atmospheric pressure", *IEEE Transactions on Plasma Science* 36, 1418-1419 (2008)

Wenting Sun, **Guo Li**, Heping Li, Chengyu Bao, Huabo Wang, Shi Zeng, Xing Gao and Hui-Ying Luo, "Characteristics of atmospheric-pressure, radio-frequency glow discharges operated with argon added ethanol", *Journal of Applied Physics* 101, 123302 (2007)

He-Ping Li, Wenting Sun, Huabo Wang, **Guo Li**, Chengyu Bao, "Electrical Features of Radio-frequency, Atmospheric-pressure, Bare-metallic-electrode Glow Discharges", *Plasma Chemistry and Plasma Processing* 27, 529-545 (2007)